On the assessment of sinking particle fluxes from in situ particle size distributions

Elena Ceballos Romero[1,2], Ken Buesseler[1], Erik Fields[3], Rainer Kiko[4,5,6], Meg Estapa[7], Lee Karp-Boss[8], Samantha Clevenger[9], Laetitia Drago[4], David A. Siegel[3,10]

[1]Woods Hole Oceanographic Institution, Department of Marine Chemistry & Geochemistry, Woods Hole, Massachusetts (USA),

[2]Department of Applied Physics II, University of Sevilla, Av. Reina Mercedes 4A, 41012, Sevilla, Spain

[3]Earth Research Institute, University of California, Santa Barbara, Santa Barbara, California (USA),

[4]Sorbonne Université, Laboratoire d'Océanographie de Villefranche, Villefranche-sur-Mer (France)

[5]GEOMAR Helmholtz Centre for Ocean Research Kiel, Kiel, Germany

[6]Faculty of Mathematics and Natural Sciences, University of Kiel, 24148 Kiel, Germany

[7]School of Marine Sciences, University of Maine, Darling Marine Center, Walpole, Maine (USA)

[8]School of Marine Sciences, University of Maine, Orono, Maine (USA)

[9]MIT-WHOI Joint Program in Oceanography, Applied Ocean Science and Engineering, Cambridge, MA, (USA)

[10]Department of Geography, University of California, Santa Barbara, Santa Barbara, California (USA)

Corresponding author: Elena Ceballos Romero (eceballos@whoi.edu)

Key Points:

- We assess the performance of UVP-based POC flux estimates using co-located sediment trap and ^{234}Th measurements from EXPORTS campaign.

- UVP flux method explains export variability between sites but not within; key issue is needing a wide POC flux range for its calibration.
- Additional data (e.g., particle morphology and transparency) are needed to improve sinking POC fluxes assessments using in situ imagery.

Abstract

The biological carbon pump is a vital component of the global carbon cycle, particularly through sinking of particulate organic carbon (POC) to the ocean interior. Particle size distribution (PSD) observations from the Underwater Vision Profiler (UVP) have been widely used to quantify sinking POC fluxes. This approach assumes that the sinking POC flux is a function of the PSD multiplied by a power law relating particle size to sinking rates and carbon content. The coefficients of the power law are quantified by regressing UVP data against sediment trap flux observations. Here, we systematically assess the performance of this approach using a large UVP dataset of co-located and coincident sediment trap and thorium-234 flux observations from the North Pacific (50°N, 145°W, August 2018) and the North Atlantic (49°N, 16.5°W, May 2021) sampled during the EXPORTS (EXport Processes in the Ocean from RemoTe Sensing) field campaign, which span both diverse environmental conditions and sinking flux values. Globally, when power law coefficients are evaluated over all sites and depths, the UVP flux method explains 80% of the variance in POC flux. However, when coefficients are determined using regional subsets of the EXPORTS dataset, the method performs poorly. Reasons include lack of knowledge of particle characteristics beyond PSD; undersampling of rare large particles; spatial and temporal scales mismatches between UVPs and flux observations; and difficulties arising from non-steady state conditions. To improve UVP-based sinking POC flux estimates regionally, additional data on particle characteristics such as transparency and morphology are needed.

Plain Language Summary

Anthropogenic CO_2 emissions drive climate change, with the oceanic biological carbon pump (BCP) playing a crucial role in mitigating its impact by transferring photosynthetically fixed carbon from the ocean surface to the deep sea via sinking particles. Understanding the BCP is essential for predicting ocean CO_2 absorption and global carbon cycle impacts. Recent advances in underwater imaging systems, like Underwater Vision Profiles (UVP), allow for tracking particle abundance and offer a means to estimate sinking carbon fluxes alongside traditional methods such as sediment traps and Thorium-234 measurements. Using data collected in the Pacific and North Atlantic oceans, this study compares UVP performance with conventional techniques, finding that while UVP provides global insights, it faces limitations at finer scales, likely due to a lack of information of particle characteristics besides their size, missing rare large particles, mismatched temporal and spatial coverage between techniques, and difficulties in understanding how the changing conditions impact particle fluxes. Ultimately, observations of the particle size distribution from underwater cameras alone do not fully capture the complexities of sinking carbon export fluxes in the ocean.

1 Introduction

The oceanic biological carbon pump (BCP) (Eppley & Peterson, 1979) drives carbon storage in the ocean's interior through the downward flux of biogenic carbon, produced by the net primary production of phytoplankton. There are multiple paths for the BCP (Boyd et al., 2019) but when considering transport to the deep ocean (>1000m) this process occurs primarily through the gravitational sinking of Particulate Organic Carbon (POC) - phytoplankton, zooplankton, detritus, and fecal pellets - from the euphotic zone to deep waters (Boyd et al., 2019; Turner, 2015). While the BCP is a well-recognized driver of atmospheric CO_2 regulation over geological timescales (De La Rocha & Passow, 2007), the precise magnitude of its current contribution to the global carbon cycle, particularly in response to human-induced changes, remains uncertain. Annual carbon export estimates by the BCP vary from 5 to >12 Gt C yr^{-1} (Boyd & Trull, 2007; Siegel et al., 2023a).

Traditional oceanographic techniques, such as sediment traps (e.g., Buesseler et al., 2007) or radioactive disequilibrium methods such as thorium-234 (^{234}Th half-life, $t_{½}$ = 24.1 d; e.g., Buesseler et al., 1992), are resource-intensive and provide limited spatial, vertical, and temporal coverage (Buesseler et al., 2007). The emergence of imaging techniques in recent decades has transformed oceanography (Lombard & Kiørboe, 2010), offering a range of tools to study properties and dynamics of particles across a range of sizes, from micrometers to centimeters, and time scales of seconds depending upon imaging protocols. These technologies, deployable on CTD rosettes from research vessels, autonomous floats, gliders, or moorings, enable observations on oceanographically relevant temporal and spatial scales, while at the same time reducing deployment costs (Giering et al., 2020). Among these, the Underwater Vision Profiler or UVP (Picheral et al., 2010) has become widely used imaging instrument because of its versatility (Kiko et al., 2022).

In situ observations of particle size distributions (PSD) from imaging platforms historically served three main purposes: 1) assessing the structural properties of planktonic food webs (Sheldon et al., 1972); 2) inferring particle sinking velocities of individual particle size classes when combined with particle collection traps equipped with polyacrylamide gels (McDonnell & Buesseler, 2010); and 3) estimating sinking particles fluxes (Guidi et al., 2008; Iversen et al., 2010; Kiko et al., 2017). In this study, we revisit and expand this third application of PSD observations using coincident and collocated sinking POC flux determinations with both traps and ^{234}Th approaches. Each of these methods has strengths and weaknesses including the spatial and temporal scales each represents. Here, we test the assumption that an instantaneous PSD imaged by UVP, essentially a stock measurement, can be related to POC flux, a rate of carbon removal on gravitationally sinking particles.

In principle, the sinking POC flux is related to the product of the particle size spectrum and a particle's sinking speed and carbon content, or:

$$POC_{flux} = \int_{D_{min}}^{D_{max}} N(D)\, \rho_{POC}(D)\, w_s(D)\, dD \qquad \text{Eq. (1),}$$

where D is diameter (mm), $N(D)$ is the number concentration of particles as a function of size in differential form (# L^{-1} mm^{-1}), $\rho_{POC}(D)$ is the POC content of a particle of size D (mg C $particle^{-1}$), $w_s(D)$ is its sinking rate (m s^{-1}), and D_{min} and D_{max} are the smallest and largest particle sizes resolved, respectively (mm). Unfortunately, we do not know a priori the size dependence of

particle sinking rates and POC content. Hence, Eq. (1) is often reformulated by combining the POC content and sinking rate terms into a power function of particle size, resulting in:

$$POC_{flux} = \int_{D_{min}}^{D_{max}} N(D)\, A\, D^{B} dD \quad \text{Eq. (2),}$$

where the coefficients, A and B, represent the combined influence of $w_s(D)$ and $\rho_{POC}(D)$, each of which follows a power-law (Alldredge, 1998; Alldredge & Gotschalk, 1988; Lombard & Kiørboe, 2010).

Guidi et al. (2008) applied equation (2) to calculate POC flux using PSDs in the 250 µm – 1.5 mm size range retrieved from UVPs by optimizing the A and B coefficients using available sinking particle flux observations from sediment traps from sites in the North Atlantic Ocean, Mediterranean Sea and South Pacific Ocean (see Table 2 in Guidi et al. (2008)). This method we will refer to as the "global UVP method" and its application assumes that the power law coefficients are valid globally. Since its introduction, the A and B coefficients from Guidi et al. (2008) have been widely applied to predict POC flux from UVP results in many studies in oceanic settings distinct from the original calibration site of the coefficients (e.g., Forest et al., 2013; Guidi et al., 2009, 2015, 2016; Ramondenc et al., 2016). Recently, Clements et al., (2022) estimated A and B using a machine learning reconstruction of global ocean PSDs determinations tuned against a global compilation of in situ sediment trap and thorium-derived particle flux observations from Bisson et al., (2018) to estimate the sinking POC fluxes from the base of the euphotic zone globally. Although previous authors have highlighted assumptions, caveats, and limitations of this approach, only a few studies (Cram et al., 2022; Fender et al., 2019; Iversen et al., 2010) have modified the global method to estimate region-specific A and B coefficients for different size ranges (see Table 1). The use of regional observations to adjust the model coefficients will be referred to here as the "regional UVP method". However, a systematic and validated approach for optimizing A and B coefficients to translate UVP-derived PSDs into accurate POC flux estimates across multiple sites and particle flux regimes remains lacking.

In this study, we use a comprehensive and unique dataset of PSD observations from UVPs, along with POC flux estimates from sediment traps and ^{234}Th that were co-located in space and time, to evaluate the performance and validity of the global and regional UVP methods. The data were collected together as part of the NASA-funded EXport Processes in the Ocean from RemoTe Sensing (EXPORTS) project at two biogeochemically contrasting sites in terms of POC flux and biogeochemical conditions (Siegel et al., 2021; Johnson et al. 2024). The present PSD datasets also cover an expanded particle size spectrum from 128 µm - 26 mm, which represents a significant broadening in both the scope and methodology of studies using in situ imagery such as UVP to assess sinking export fluxes in the ocean.

2 Materials and Methods

2.1 Deployments and Setting

The goal of the EXPORTS field campaign is to develop a predictive understanding of the export, fate, and carbon cycle impacts of global ocean net primary production and to assess their impacts in contemporary and future climates (Siegel et al., 2016). Two field campaigns were carried out in two vastly different ocean ecosystems encompassing a wide range of environmental

conditions: 1) the North Pacific (NP) at Ocean Station Papa (OSP, 50°N, 145°W) in August-September 2018, and 2) the North Atlantic (NA) in the vicinity of the Porcupine Abyssal Plains Sustained Observatory (PAP, 49°N, 16.5°W) in May 2021. In both field deployments, operations were conducted in three consecutive sampling cycles or "epochs" (E1, E2, and E3 from hereafter) designed to constrain the pathways for organic carbon transformation and export. The length of each epoch was approximately one week with the goal of completing a sequence of observations that could be repeated three times during a given cruise. Conceptually, the aim is to follow how surface properties might be observed to propagate to depth as part of the BCP, i.e., a particle formed at the surface on day 1, would take approximately one week to reach 500 m if settling at roughly 70 m/d (Siegel et al., 2021).

The North Pacific site can be characterized as an iron-limited, high-nutrient, low-chlorophyll (HNLC) region of the world ocean, which leads to limited phytoplankton production and surface chlorophyll (Chl-a) concentrations. An overview of the NP sampling plan, including context information on physical and bio-optical properties, nutrients, and phytoplankton biomass, is presented in Siegel et al. (2021). Two ships were deployed during the NP expedition: a Process Ship (*R/V Roger Revelle*, cruise *RR1813*) focused on sampling biogeochemical stocks and fluxes while following a Lagrangian float, and a Survey Ship (*R/V Sally Ride*, cruise *SR1812*) that characterized the spatial distribution of properties surrounding the Process Ship and cross-calibrated sensors onboard the ships and the autonomous platforms (Siegel et al., 2021). Briefly, during our study period the oceanographic setting was typical of late-summer conditions at OSP with low biomass, a highly recycled food web, and low sinking POC export fluxes driven largely by zooplankton processes (McNair et al., 2023; Stamieszkin et al., 2021; Steinberg et al., 2023). Weak horizontal currents and spatial gradients in biogeochemical fields and low level of temporal variability characterized the three sampling epochs (E): E1 (August 14-23), E2 (August 24-31), and E3 (September 1-9). In terms of POC export, the site was characterized by a modest sinking carbon fluxes with an export efficiency at the base of the euphotic zone (ratio of POC flux to net primary production) of ~13% and a flux attenuation in the subsequent 100 m of ~39% (Buesseler et al., 2020a).

The North Atlantic site is a highly advective environment dominated by eddies which can cause upper ocean biogeochemical properties to evolve on time and space scales comparable to those driven by biological processes (Johnson et al., 2024). The NA operations were conducted in a coherent, anticyclonic, physically retentive eddy that minimized horizontal exchanges, so that changes in biological or chemical properties were dominated by local rather than advective processes (Johnson et al. 2024). During the NA deployment, a third ship was added to the Survey Ship (*RSS Discovery*, cruise *DY131*) and the Process Ship (*R/V James Cook*, cruise *JC214*), the *R/V Sarmiento de Gamboa* (cruise *SdG2105*), that focused on plankton and metazoan imaging. Similar to the NP sensor calibration exercise, a detailed intercalibration was performed on all the NA sensor observations (Siegel et al., 2023b) . In short, the expedition sampled a transition to high sinking particle fluxes as conditions differed for the three sampled epochs. The first epoch (E1; May 5-7) was marked by a very large diatom biomass in the surface ocean but an absence of aggregates in the upper mesopelagic portion of the water column (Romanelli et al., 2024; Siegel et al., 2025). The second epoch (E2; May 11-20) followed a major storm with wind speeds exceeding 40 knots and was marked by a large change in surface properties and the appearance

of aggregates. Export flux metrics remained low by most measures until the third epoch (E3; May 21-29), which was marked by large increases in both sinking particle fluxes and aggregate abundances (see Brzezinski et al., 2024; Clevenger et al., 2024; Romanelli et al., 2024; Siegel et al., 2025).

2.2 Measurements and Biogeochemical Context During EXPORTS

Sediment trap fluxes: Two types of sediment traps with identical collection tubes (collection area = 0.0226 m^2) were used - neutrally buoyant sediment traps (NBSTs) and a surface-tethered sediment trap array (STT). Sinking particles were collected over approximately 2 to 5-day deployments in the upper 500 m of the ocean during the three epochs in each EXPORTS field campaign (Estapa et al., 2021; Johnson et al., 2024). Results from these traps are discussed here without distinction of trap type. Formalin-poisoned brine traps were gravity filtered through 335-micron screens, swimmers were manually removed from the screens under magnification, and the remaining material was recombined with < 335 µm material for bulk elemental analysis for POC. During the NP, sample composition was used to perform an additional correction for POC from small swimmers that could not be removed following screening (Estapa et al., 2021). POC fluxes were modest during E1 and E2, and increased moderately during E3. During NA, particle export flux seen in the traps increased rapidly two weeks after the experiment started, from similarly low fluxes in E1 and E2 to high fluxes in E3, suggesting strong temporal variability in flux (Clevenger et al., 2024; Romanelli et al., 2024).

234-Thorium POC fluxes: The ^{234}Th disequilibrium relative to uranium-238 (^{238}U) in depths ranging from 0 to 500 m was used during EXPORTS to estimate POC fluxes following the methodological approach proposed by Buesseler et al. (1992). A description of the analytical method can be found in Clevenger et al. (2021). A full description of ^{234}Th measurements and derived fluxes from the NP and NA experiments can be found in Buesseler et al. (2020a) and Clevenger et al., (2024), respectively.

During the NP, the spatiotemporal variability of ^{234}Th activity was fairly consistent within each epoch, which supported the use of a steady state interpretation of the deficits (Buesseler et al., 2020a), an approach that reduces uncertainties related to error propagation over short timescales (Ceballos-Romero et al., 2018; Savoye et al., 2006). The NP ^{234}Th observations show relatively homogenous and consistent ^{234}Th disequilibria, with higher ^{234}Th fluxes observed at depths of 50 to 100 m, remaining relatively constant or decreasing at greater depths in the water column (see Figures 1 and 2 in Buesseler et al., (2020a)). ^{234}Th-derived POC fluxes showed a similar trend, but with fluxes decreasing more sharply with increasing depth during all epochs.

During NA, the magnitude of ^{234}Th disequilibria varied both temporally and spatially through the cruise. However, ^{234}Th-derived POC fluxes revealed minimal to no attenuation with depth across all three epochs, with fluxes at 100 m persisting with similar or even slightly higher values at deeper waters (see Figure 3 in Clevenger et al., 2024). Existing ^{234}Th deficits indicated that particle fluxes had been high prior to the start of the cruise (Clevenger et al., 2024). Since ^{234}Th measurements are integrated over time rather than an instantaneous representation of a system, a non-steady state model was needed to derive POC fluxes that increased during the experiment.

In Situ Observations of Particle Size Spectra: The 5th generation of underwater cameras (UVP5; Picheral et al., (2010)) was used to collect all PSD data used here. A total of 387 high-resolution, full depth profiles of particle size spectra were sampled with five different UVPs mounted on the bottom of each ship CTD-Rosette (169 and 218 in the NP and NA, respectively; see Table 1). The UVP5 captures and processes images of particles (living and non-living) in real time at a rate up to 6 Hz using two collimated red light-emitting diodes (LEDs) that illuminate a well-defined volume of ~1 L with each 100 µs flash. Particles are detected and sized based on their projected area and converted to equivalent spherical diameter (ESD). Here, particle counts and binned into logarithmically distributed size bins ranging from 128 µm to 26 mm, although it is recognized the largest few bins will very rarely if ever contain any particles. This range of bins was chosen to ensure consistent data quality and comparability across the five UVP5 units used (details on the UVP5 intercalibration procedure are available in Siegel et al., (2023b) and summarized in the Supporting Information, SI; Section S1). Particle counts were obtained from the downcast of each CTD cast, converted to particle size spectra, $N(D)$, by normalizing by bin width and then aggregated into 5-m depth averages. Based upon the CTD's lowering rate (~1 m s^{-1}), the UVP5's sampling rate (20 Hz) and its sampling volume (~1 L), it is estimated that each 5-m PSD determination represents an average of ~100 L.

2.3 Determination of Sinking POC Fluxes from UVP PSD Observations

We estimate the values and uncertainties for the coefficients *A* and *B* in equation (2) using independent POC flux estimates from both trap and ^{234}Th fluxes using a nonlinear least squares regression procedure. Fits were made using all available EXPORTS observations and depths, the "global UVP method" as well as using data from the NA and NP deployments separately, the "regional UVP method". Initial work fitting coefficients for individual epochs were conducted, but the results were poor; likely due to the very limited number of data points available (as few as 5 for ^{234}Th and 9 for sediment traps; Table S1), Several considerations arise concerning how data are used to fit coefficients A and B, including the UVP size range selected for fitting, the selection of UVP and flux determinations to be used, and the vertical resolution used.

Particle size range considerations - Guidi et al. (2008)'s original application of the UVP flux method used data from older UVP models (UVPs 2, 3, and 4) that were processed into in an overlapping size range from 0.25 to 1.5 mm across 8 standardized size bins (see Tables 2 and 3 in Guidi et al., (2008) for details). With advances in the UVP5 model (Picheral et al., 2010), a wider size range of sizes are available from 128 µm to 26 mm across 23 standardized size bins. The wider range of bins is used as larger particle sizes which should make a greater contribution to the total POC flux (Durkin et al., 2021; Laurenceau-Cornec et al., 2020) and hence, the potential for better performance. To compare with the original study by Guidi et al., (2008), we did a global optimization using the original 8 size bins with the EXPORTS data set. For all cases, we did not attempt to correct for potential all living and non-living particles, consistent with most previous studies.

Sediment trap considerations - For the consideration of the spatial scales for the NP traps, we only matched UVP profiles and trap fluxes from the same source funnel, as described in Estapa et al., (2021). In essence, choosing only UVP profiles falling within the particle source region

defined by local currents and assuming a conservative particle sinking rate of 100 m d^{-1} (e.g., Siegel et al. 2008). In the NA, the spatial criterion was related to the dimensions of the core of a retentive eddy that was sampled during the experiment in a Lagrangian fashion (Erickson et al., 2023; Johnson et al., 2024). In this case, only UVP profiles and trap flux observations within the eddy center waters were used (defined as ≤ 15 km from the analyzed eddy center; Johnson et al. 2024).

Thorium-234 flux considerations - As both UVP images and ^{234}Th samples were collected on the same CTD cast, paired UVP and ^{234}Th observations were used to construct the global (both NA and NP) and regional (NP or NA separately) estimates of *A* and *B*. All available pairs were used in the NP as there was little discernable spatial variability (Buesseler et al., 2020a). However, for the NA, we restricted the ^{234}Th and UVP matchups to the eddy center, consistent with the approach used for the trap data.

Vertical Resolution Considerations - The three data sets used all have different vertical resolutions in their sampling. For comparisons to a specific trap depth or ^{234}Th measurement, we used the average of the 5-m resolution UVP data at the measurement depth and the three 5-m depth intervals above it. This resulted in a 20-m depth average, corresponding to imaging roughly 400 L of seawater. No data above the mixed layer depth (MLD) were considered, as this layer typically marks the upper boundary for net particle export from the surface ocean. This is especially true when the MLD is deeper than the particle production zone, in which case suspended and sinking particles are physically mixed below the euphotic zone (Buesseler et al., 2020b).

Optimization procedure and uncertainty calculations – Estimates of the *A* and *B* coefficients were determined using the *nlnfit.m* routine in Matlab (Natick, MA, USA), which uses the Levenberg-Marquardt algorithm (Seber & Wild, 2003). Uncertainty bounds are calculated as the 95% confidence intervals using the variance-covariance matrix of the fitted coefficients. Confidence intervals for the fit parameters and several goodness of fit metrics, such as the coefficient of determination for the linear fit (r^2), the normalized root mean square error (nRMSE), are reported in Table 1. The mean bias was calculated, but it is omitted from Table 1 because it was zero.

We note that, as highlighted in Clements et al., (2023), the coefficients *A* and *B* are not entirely independent during fitting, and compensation between the two can lead to similar flux estimates from different parameter combinations. This trade-off introduces uncertainty in the interpretation of A and B and suggests that any comparisons of their values should be made with caution. In this study, our focus remains on how optimized combinations of A and B reproduce observed POC fluxes rather than interpreting the coefficients individually.

3 Results

3.1 PSD Observations

Example profiles PSD spectrum of in situ particle abundance (# L^{-1} mm^{-1}) as a function of ESD (mm) and depth are shown in Figure 1. In the NP, UVP-PSD observations exhibit little discernible

temporal variations (Figure 1a and S1a). Conversely, in the NA, PSDs changed throughout the cruise (Figure 1b, 1c, and S1b).

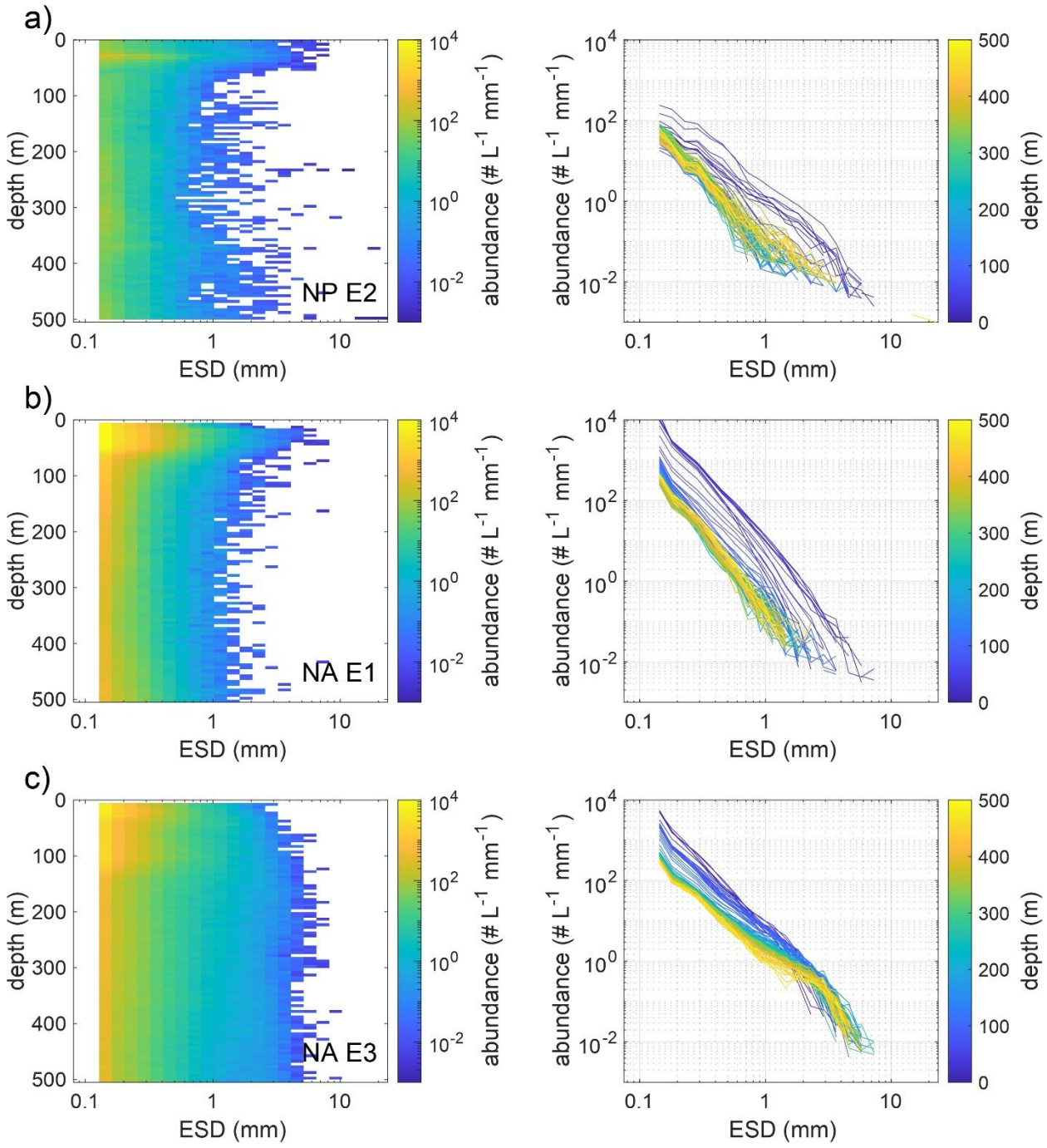

Figure 1. Example particle size distribution (PSD) profiles for selected epochs plotted against aggregate equivalent spherical diameter (ESD, mm) and depth for the a) NP and b-c) NA. For each panel, the figure on the left shows ESD versus depth, the color bar indicates particle abundance for each size (in # L^{-1} mm^{-1}, logarithmic scale). Red indicates a higher number of particles than blue. The figure on the right shows ESD versus abundance, the color bar indicates depth (m). Red indicates deeper waters than blue. For the NP, few discernable changes in PSD were observed over time and a random profile in E2 was chosen. For the NA, PSD evolved between epochs and representative profiles early (E1) and late (E3) in the cruise are shown.

As expected, particle abundance decreases with increasing size for all casts in both experiments, with smaller particles being more abundant than large ones by several orders of magnitude at all depths. However, distinct vertical patterns emerge for each experiment based on the particle size. Note also that there very few particles measured by the UVP with ESD > 5 mm.

In the NP, abundances of small particles remain relatively consistent across depths and time, whereas larger particles decreased in abundance with depth and were constant at lower abundances below 100 m (see right panel in Figure 1a). In the NA, the PSD changed both over time and depth (see Figure 1b and 1c). During the initial days of the experiment (E1), small particles were highly concentrated in the surface layer (0-50 m) and decreased with depth, while deeper layers showed a shift toward fewer, larger particles. In the later stages of the experiment (E3), there was a substantial increase in large particles, especially at depth.

3.1 *A* and *B* Coefficients using EXPORTS Results

When applying the global approach using traps, i.e. calibrating all data from both sites for a single *A* and *B* value, no significant differences were observed within the uncertainty bounds in the retrieved *A* and *B* coefficients using either 8 or 23 size bins (Table 1). However, the ratio of uncertainty to estimate is > 1 for the 8 bins (SI, Figure S2). Hence, we only consider 23 size bin models in our comparisons below (A = 13.98 ± 5.78 mg C d^{-1} mm^{1-B}, B = 1.59 ± 0.44, r^2 = 0.83, Figure 2a). When applied to ^{234}Th POC flux determinations, the global model has a poorer fit with a somewhat larger value of A though a similar B (A = 19.36 ± 2.85 mg C d^{-1} mm^{1-B}, B = 1.38 ± 0.15, r^2 = 0.56; Figure 2b). Using sediment traps, the NA regional approach produced A and B coefficients similar to those from the global approach, with differences falling within uncertainty bounds. However, in the NP, the regional model showed no predictive power using traps (r^2 = 0.04). When using ^{234}Th, neither the NP or NA exhibited regional predictive capability (r^2 = 0.08 and 0.02, respectively; Table 1).

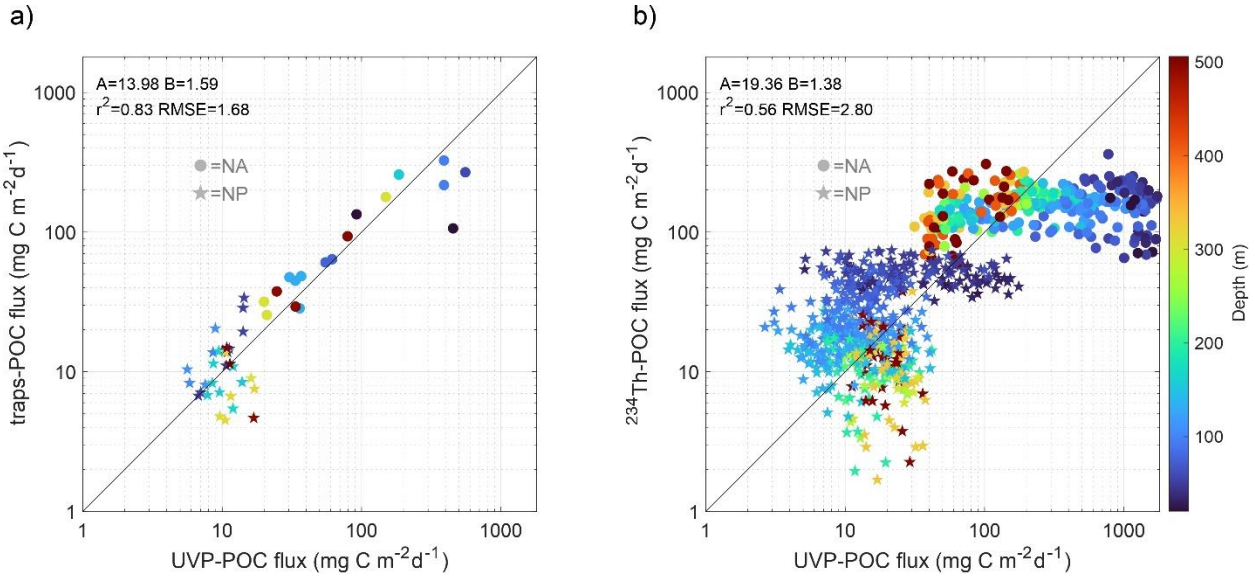

Figure 2. Results of the global models for UVP-based POC fluxes (in mg C m^{-2} d^{-1}, x-axis) using a) traps and b) ^{234}Th (y-axis) using the global approach for 23 size bins (128 µm – 26 mm). Indicated in each panel along with the r^2 of the linear fit and the nRMSE. The biases are not shown because they are zero for all fits. Goodness of fit statistics

and 95% CIs for the A and B coefficients are provided in Table 1. Stars represent the NP results, and circles the NA results, with color representing depth (in m). The black line indicates the 1:1 line.

3.1 Vertical Profiles of POC flux

Using the *A* and *B* values from EXPORTS, we can derive vertical profiles of POC flux from any given UVP profile in that study (Table 1). Figures 3 and 4 show the variability in UVP derived flux profiles for both the global (panels a and e) and regional (panels b-d and f-h) fit parameters for the NP and NA, respectively. Concurrent trap and ^{234}Th flux profile observations are overlain in the upper and lower rows of Figures 3 and 4, respectively. In each case, the flux profiles using UVP data show both extreme vertical variability and large cast to cast variability (red lines).

For the NP, UVP fluxes range from 5 to 50 mg m^2 d^{-1} (global calibration against all traps; Figure 3a), with an average around 50 mg m^2 d^{-1} below the MLD decreasing to vertically uniform values of ~ 10 mg m^2 d^{-1} below 100 m. Note however individual UVP casts even in the upper 50-100 m can have lower or higher fluxes predicted than these averages. The fit of the UVP average with the observational trap results in the NP is good within the spread of the trap data (Figure 3a). Similar patterns are found for the UVP fluxes calibrated with the ^{234}Th observations, although the fluxes are > 1.5 times higher, reflecting the higher values of A used (Figure 3d).

In principle, a regional calibration of *A* and *B* and concurrent UVP and flux observations might be expected to improve the matchups; however, that is not the case. Using regionally derived models for the NP separated by epoch (Figures 3b-d), the UVP POC flux exceeds the traps around 350 m in E1 and E2 (Figures 3b and 3c), and the increase in trap flux in E3 at 100 m is not captured in the E3 UVP profiles (Figure 3d). Small scale changes in flux versus depth or time are thus not improved by using a regional fit to the NP trap data. Considering the NP regional model derived from ^{234}Th, individual ^{234}Th flux profiles vary cast to cast, but not over as wide a range as the UVP derived fluxes (Figures 3f-h). A decrease in flux versus depth is seen in both UVP and ^{234}Th results, but with the UVP showing higher values on average at deeper depths (Figure 3e). A subsurface peak at a depth of ~350 m is observed in the ^{234}Th optimized UVP fluxes for all three epochs and is especially strong in the NP E1 (Figure 3f), which may be related to zooplankton diel vertical migration, a process that Amaral et al., (2022) , using inversion analysis of large volume pumped POC samples, showed can significantly contribute to large particle flux in the upper mesopelagic (see their Figure 12). Also, while ^{234}Th fluxes generally increase to some maximum value in the subsurface (here 50 m) and then decrease, UVP derived fluxes always are highest in the shallowest depths.

In the NA, applying the global trap-based model to UVP data yields flux estimates that are larger and more variable than in the NP (Figure 4a). As noted previously, the progression of the bloom resulted in large local changes in particle properties, and this is illustrated clearly when the NA results are displayed for each epoch. Using the NA regional calibration of the UVP data with traps, there is a better fit between UVP fluxes and traps if broken down by epoch, for which the flux values increase dramatically in E3, especially at depths > 100 m (Figures 4e versus Figures 4c and 4d).

The global model using ^{234}Th data in the NA results in higher UVP fluxes on average (Figure 4e) and a predicted increase in flux using matched UVP profiles and regional model in E3 (Figure 4,

panels f-h). However, the shape of the two flux profiles differs, with a higher flux at the surface and steeper flux attenuation evident in the UVP data but not in ^{234}Th results.

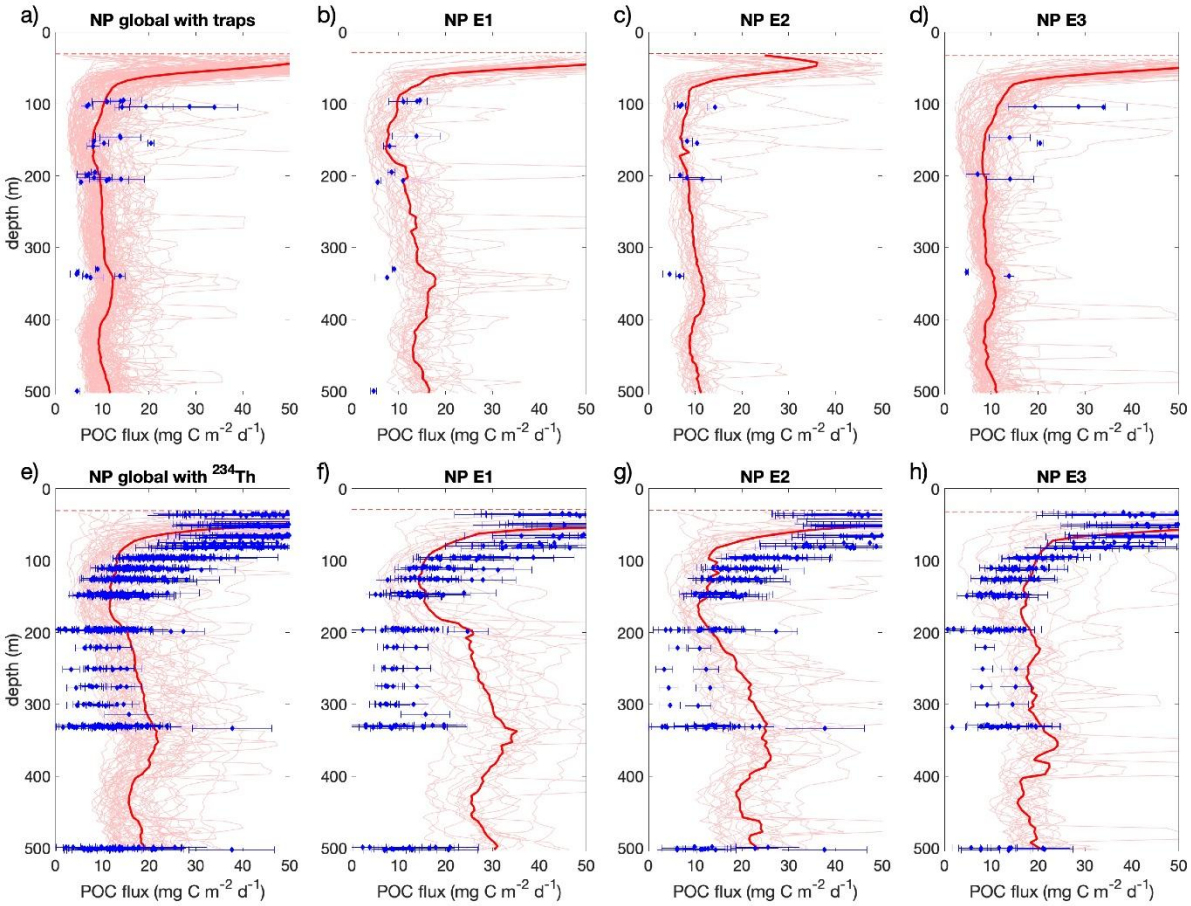

Figure 3. Vertical profiles of POC fluxes for (a) the global and (b-d) regional approaches in the NP using traps grouped by epochs: E1, E2, and E3 (from left to right) where the blue diamonds denote sediment trap POC fluxes with uncertainties from Estapa et al., (2021). Panels (e-h) show the corresponding UVP fluxes optimized using ^{234}Th data while the gray lines show the ^{234}Th-derived POC flux and the fluxes for each cast, and the black lines show the mean flux. The horizontal dashed line indicates the mean mixed layer depth over the course of the experiment. Pink lines show the UVP-based POC flux for each UVP cast, calculated using the A and B coefficients derived from each approach. Only UVP casts paired with trap or ^{234}Th profiles that fall within an epoch are shown. In panels (a) and (e) the red line represents the cruise mean UVP-based POC flux of all casts used for the fitting, which includes casts within a 100 md^{-1} source funnel region (see main text for details). In the rest of the panels, the red line indicates the epoch mean.

4 Discussion

We set out to assess the quality of POC flux estimates derived from the UVP imagery using concurrent sediment traps and ^{234}Th flux observations from the EXPORTS field campaign. The challenges are substantial given the multitude of issues presented. First, UVP PSD determinations are at best measures of sinking and non-sinking particles and living stocks, within certain size ranges and over scales set by the number of images (Hz), imaging volume (liters) and duration of a CTD cast (hours; meters) (Picheral et al., 2010; 2022). Traps measure the gravitational sinking

flux of particles, largely non-living, and originating from a large particle source area (Siegel et al., 2008) determined by sinking rates, currents and deployment durations (several days; 10's km^2). Biases in trap fluxes occur due to hydrodynamics, swimmers, preservation and other issues (Buesseler et al., 2007). The ^{234}Th flux method tracks small scale variations in flux (km) but averaged over days to weeks. The ^{234}Th-derived POC flux depends on the measured ^{234}Th disequilibrium and generally ignores physical processes, but importantly here, the flux can be sensitive to whether a system is at steady state or not, over the course of its half-life (24.1 d) (Ceballos-Romero et al., 2018; Clevenger et al., 2024; Savoye et al., 2006). A conversion from ^{234}Th flux to POC flux also requires consideration of observed variations in its ratio to POC on particles that vary with depth and location (Buesseler et al., 2006). So, mismatches between UVP, trap and ^{234}Th estimates of POC flux are expected to be due to a combination of methodological consideration and their respective spatial and temporal averaging.

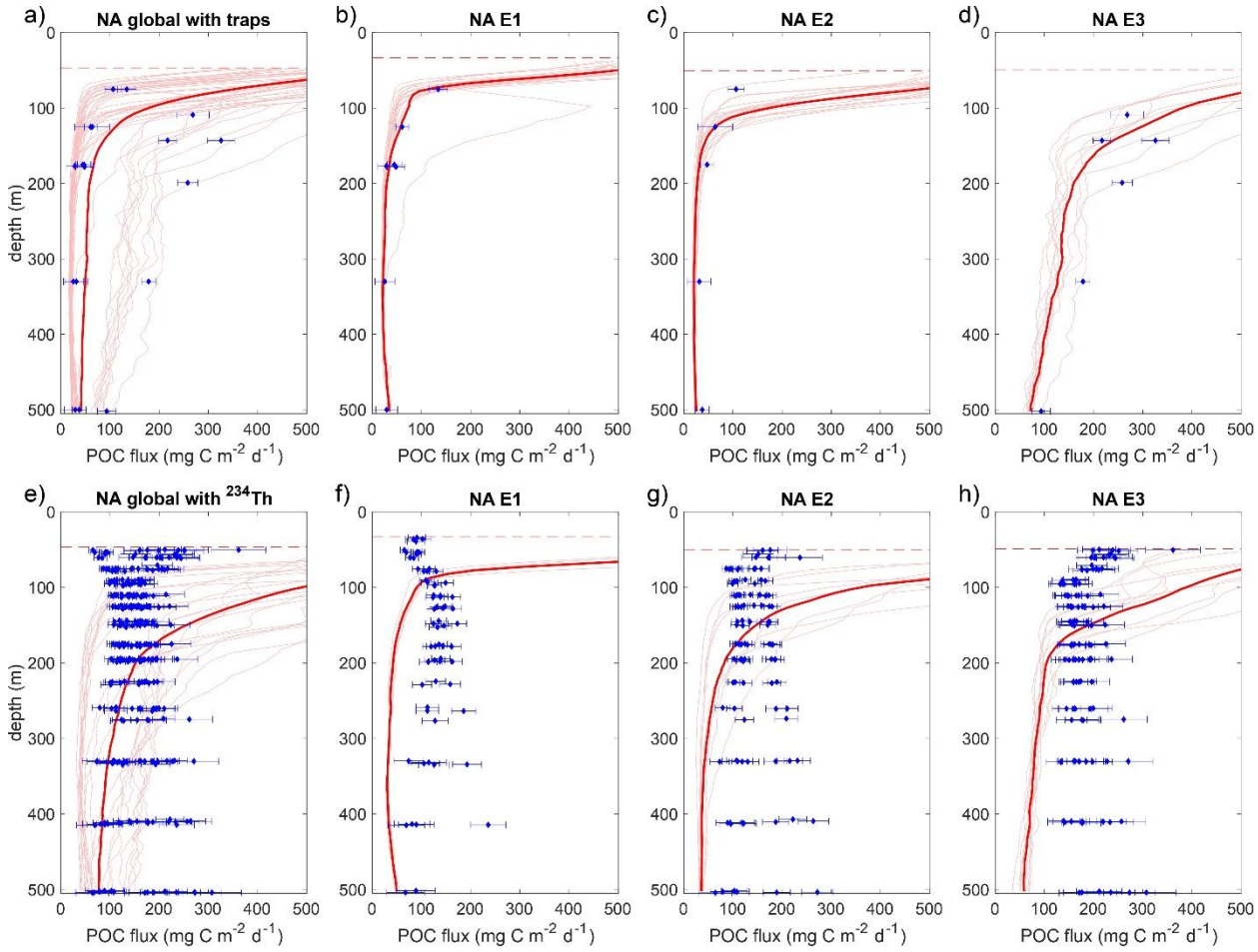

Figure 4. Corresponding figure to Figure 3 for the NA deployment. Casts used for the fitting include only those within the eddy center.

The EXPORTS project provides a unique opportunity to evaluate the utility of UVP-derived flux estimates using an extensive set of co-located and simultaneous sediment traps and ^{234}Th observations. A key finding is that UVPs can be effectively trained to translate observed PSD

changes into POC fluxes when the range in POC fluxes spans several orders of magnitude, and when stocks and fluxes are roughly near steady state. However, when POC flux variations are smaller than an order of magnitude, i.e., at local scales, or are in non-steady state conditions, UVP flux determinations can have large uncertainties. Here, we delve into the findings that led us to these insights.

4.1 Comparisons of Global Models

The globally optimized A and B coefficients found during EXPORTS using traps were 13.98 and 15.44 for A, and from 0.73 are 1.59 for B, respectively for the 8 and 23 size bin models (Table 1). Other global estimates from Clements et al., (2023); Guidi et al., (2008); and Kriest (2002) range from 12.5 to 18.0 for A, and 2.2 to 3.8 for B (Table 1). All of these have considerable uncertainty, particularly for our estimate derived using only 8 size bins.

Importantly, our analysis shows that even small differences in the *A* and *B* coefficients lead to significant differences in POC fluxes predicted from UVP data (Figure 5), despite the potential compensation between the two parameter values during fitting (Clements et al., 2023). These differences are primarily driven by the B coefficient, which is more sensitive to the particle size range than the A coefficient. Applying the global *A* and *B* values derived by Guidi et al., (2008) to our data consistently underestimates trap-measured POC fluxes by an order of magnitude, particularly at lower flux values (Figure 5). Using regionally derived *A* and *B* coefficients leads to even larger differences, as shown by applying regional models from the NP and the NA in EXPORTS, as well as from previous studies such as Iversen et al. (2010), Fender et al. (2019), or Forest et al. (2013). However, the comparison is excellent using Clements et al., (2023)'s *A* and *B* coefficients applied to the EXPORTS data set.

We attribute differences in the *A* and *B* coefficients primarily to differences in particle characteristics found during the EXPORTS deployments, compared to the prior studies (SI, Figure S3). In particular, different depth ranges were considered, which is especially important since a single A and B values are applied at all depths. Both Guidi et al. (2008) and Iversen et al. (2010) focused on deeper sinking aggregates (100–1000 m, and 1200-1900 m depth respectively) than our study (MLD - 500 m depth). Coefficient *A* represents the product of sinking speed and POC content, while coefficient *B* is linked to the fractal dimension, which describes particle shape complexity. An increase in fractal dimension with depth implies a decrease in particle porosity (Logan & Wilkinson, 1990), which could account for their higher B values (3.81 and 4.27, respectively), as the physical compression of aggregates can compact them decrease porosity (Logan & Kilps, 1995). Our EXPORTS results, which show lower B values (all values <1.6), suggest the presence of more porous particles, likely aggregates, in the upper 500 m for both the NP and NA deployments.

We also considered whether changes in *A* and *B* reflect genuine variations in particle characteristics rather than an artifact of the size range used by the imaging systems in different studies. Our 8 bin size range was chosen to match Guidi et al. (2008), and yet Guidi et al. (2008)'s *B* value is 5 times higher (3.81 versus 0.73; Table 1). Therefore, we do not think size range is the primary reason here for differences in *A* or *B* values, rather it is more likely to be attributed to unaccounted for differences in particle characteristics.

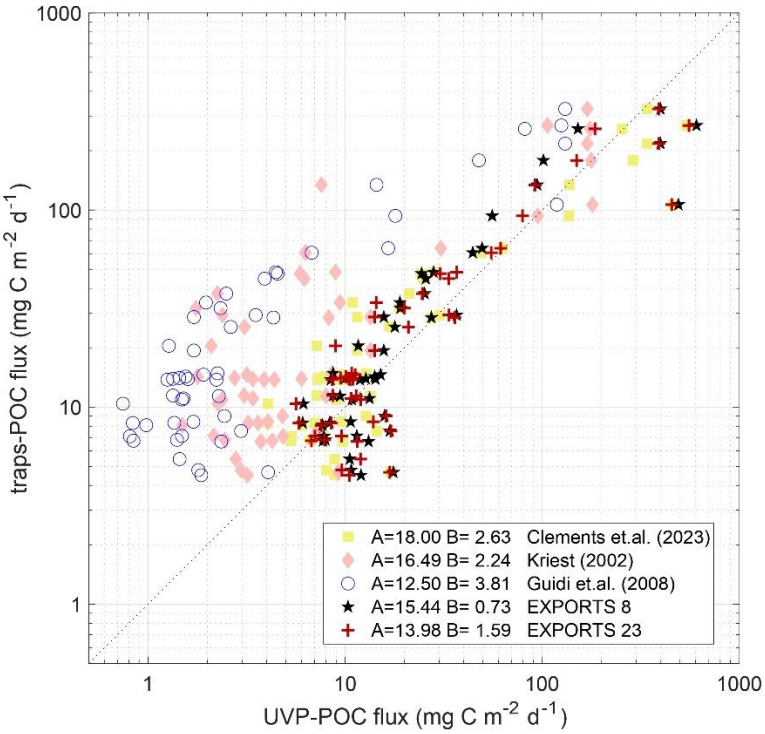

Figure 5. Results of the matchups between UVP-based POC fluxes (in mg m^{-2} d^{-1}, x-axis) and sediment trap fluxes (y-axis) using five different sets of A and B coefficients from previous studies and our own, applied to the entire EXPORTS data set. The coefficients used are from: 1) Clements et al. (2023) (yellow squares), 2) Kriest (2002) (orange diamond), 3) Guidi et al. (2008) (blue circles), and the coefficients obtained in our study for the global approach using traps with 4) the same 8 size bins as used by Guidi et al. (2008) (black stars), and 5) 23 size bins (red cruxes; See Table 1).

Another aspect of UVP size ranges is that, at the smaller end, there can be an undercount of the more abundant particles as one reaches the resolution limit (Stemmann & Boss, 2012). Here, the smallest bin considered is 128 µm, which is several times larger than typical pixel size of UVP5 imagery (Picheral et al., 2010), so this should not be an issue. Importantly, about 50% of the cumulative particle size distribution occurs near 0.2 mm ESD (see Figures 1 and S1), indicating that the calculated flux is strongly dominated by these smaller particles. At the larger size ranges, > 0.8 mm to 26 mm, the total particle counts drop off and only rarely are particles larger than 10 mm observed (Figures 1 and S1). One reason we combine UVP images into 20-m depth bins before the fit parameters are calculated is to increase imaging volume, and hence our chances quantifying these larger size bins.

The size dependence of the globally modeled trap POC fluxes (i.e., the integrand of Eq. (2)) shows that the particle size contribution to the total POC flux varies across depths, epochs, and regions (SI, Figure S4). In the NP, particles larger than 1 mm contribute more substantially to the modeled POC fluxes, especially in shallower waters (~50% of flux), compared to mid and deep waters (~20-40% of flux). In the early stages of the NA sampling, about half of estimated POC fluxes is contributed by particles smaller than ~0.3 mm, and particles sizes larger than 1 mm do not contribute more than 10% of the total POC flux. As the bloom developed (E3), particles larger than 1 mm contribute about half of the modeled POC flux at depths below ~250 m, highlighting the importance of large aggregates in driving export.

4.2 Comparisons of Regional Models

Our assumption in creating the regional UVP flux models was that regional differences in particle characteristics would influence the retrieved values for the *A* and *B* coefficients. However, optimizing the *A* and *B* parameters to regional data sets led to higher uncertainty in UVP-based POC fluxes (Table 1). This is likely due to the smaller range of flux values found within each regional subset. Thus, while UVP flux calibration can still be done at regional levels, results should be interpreted carefully. For instance, we attribute the lack of predictive power in the regional calibration in the NP - regardless of whether traps or ^{234}Th are used (Table 1) - to the minimal spatial and temporal variations in POC flux during the experiment. In the NA we see a higher range and variation in POC flux, which improved the flux calibrations using UVP and traps (Table 1). In sum, we consider UVPs well-suited for understanding large scale POC flux differences across multiple orders of magnitude; however, this approach is less effective at refining small-scale or short-term export rates, especially if strong flux variations do not occur locally or temporally.

4.3 Assessing the UVP Modeled POC Fluxes versus Depth

4.3.1 Insights from the NP

The UVP fluxes, whether derived from global or regional models optimized using trap or ^{234}Th fluxes, performed poorly for the NP (Table 1). During the NP deployment, temporal changes in export were minimal, and the system exhibited largely steady state conditions in water mass properties, production rates, chlorophyll concentrations, particle stocks (McNair et al., 2023; Siegel et al., 2021), and UVP PSD profiles (Figures 1, 3 and S1). Both trap and ^{234}Th results show no noteworthy changes in POC fluxes between E1 and E2, with only small increases detected by traps in E3 (Buesseler et al., 2020a; Estapa et al., 2021). This suggests that conditions in the NP were relatively constant with respect to POC fluxes.

Sinking particle characteristics during the NP deployment varied both with depth and across the three deployment periods (Durkin et al., 2021; McNair et al., 2023). Further much of the sinking POC flux was in the form of small particles driven by mesozooplankton processesing (Durkin et al., 2021; Amaral et al. 2022; McNair et al., 2023; Shea et al. 2023), as marine snow aggregates (> 0.5 mm) were not found in any of the Marine Snow Catcher deployments (Romanelli et al., 2024). Durkin et al., (2021) used sediment traps equipped with polyacrylamide gel layers found that small particles (< 100 µm) contributed on average 17% (± 9% s.d.) of total POC flux in the upper 500 m. However, Estapa et al., (2021) concluded that traps undercollected small particles due to hydrodynamic effects (Buesseler et al., 2007), suggesting that the contribution of particles too small to be sampled by the UVP may have been higher. This may be an issue as flux values calculated from UVPs are highly sensitive to small particle abundances (Bisson et al., 2022). Recent work by Clements et al., (2023) has demonstrated that extending the UVP's size range to smaller sizes using power-law extrapolation reduced bias in flux estimates and this procedure should be considered in future work.

Large marine snow-sized (≥ 5 mm) aggregates were rarely, if ever, sampled by the UVPs during the NP deployment (Figures 1 and S1). However, it was observed that the rare occurrence of salps and their very large fecal pellets (≥ 4 mm; see Figure 2d in Steinberg et al., (2023)) had an

inordinately large contribution to sinking POC fluxes (Durkin et al., 2021; Steinberg et al., 2023). Notably, during E1, salp fecal pellet export contributed 48 to nearly 90% of the modeled total POC flux (Steinberg et al., 2023), which happens to coincide with the largest discrepancies between UVP-based and ^{234}Th-derived POC fluxes and, to a lower extent, traps (Figure 3f). The UVPs rarely observed large salp pellets due to the ephemeral occurrence of salp populations, their rapid sinking speeds and the relatively small sampling volume of the UVP (Steinberg et al., 2023). Thus, significant underestimation of POC flux due to the potential under sampling of salp fecal pellets by UVP imaging likely would lead to misleading conclusions about carbon export dynamics. Estapa et al., (2021) also concluded that traps under collected rare larger particles, including salp fecal pellets, which would make the trap POC flux results too low. The ephemeral nature of salp populations and their impacts on sinking POC fluxes may also explain the fluctuating nature of UVP-derived POC flux profiles versus depth and their large cast-to-cast variations (Figure 3).

It should also mentioned that the detection of rare living organisms by the UVP will introduce uncertainty into flux calculations (Bisson et al., 2022). For example, Kiko et al., (2020) found that excluding living organisms and artifacts larger than 1 mm from the UVP5 dataset decreased the variability of PSD-derived POC flux estimates. Here, morphological classifications of UVP images were made of the EXPORTS NP UVP data used to develop POC flux models found a low contribution from living organisms (~9%) from the total number of particles larger than 1 mm imaged (A. McDonnell, pers. comm., 2020). Although it is small, the fraction of large particles that were living in the NP is considerably larger than what was found in the NA (< 1%; Drago, 2023). Again, the observations of these very large particles in UVP5 PSD will be rare, thereby minimally influencing the uncertainties in UVP flux determinations (Bisson et al., 2022; Kiko et al., 2020).

4.3.2 Insights from the NA

As the NA deployment was highly dynamic taking place during the demise of the North Atlantic spring bloom (Johnson et al., 2024; Romanelli et al., 2024; Siegel et al., 2025), discrepancies in the UVP-based POC fluxes are likely due to temporal factors (SI, Figure S5). Briefly, during E1 (May 5-7, storm 1 on May 7-11), export fluxes were low across most measures, including sediment traps and ^{234}Th (Figure 4), and no aggregates were found in the Marine Snow Catcher (Romanelli et al., 2024). After storm 2 (May 15) in E2 (May 11-20), aggregates were collected in the Marine Snow Catchers, but export fluxes increased some, until E3 (May 21-29), when large particles substantially increased, particularly at depth (Fig 4; see also Figure 2a in (Romanelli et al., 2024). Shifts in the dominant plankton community, from large diatoms to a more diverse phytoplankton community were also observed (Meyer et al. 2024; San Soucie et al. 2024). Throughout the NA experiment, particles were consistently fluffy and porous, becoming progressively fluffier and more porous as the cruise progressed (Siegel et al., 2025). Analysis of the morphology of individual large (≥ 1 mm) particles sampled in the images collected by the UVP showed that fluffy aggregates dominated the dataset, accounting for 88% of the particles analyzed, while dense aggregates (10%), fecal pellets (1%), zooplankton pellets (1%) and living organisms (0.7%) made up the rest (Drago, 2023).

Given the evolving conditions, the average of the UVP profiles effectively captured the bloom stages, mirroring the trap results, both of which increased in E3 (Figures 4a-d). POC fluxes from the traps varied by an order of magnitude between E1 and E3, which allowed us to effectively train UVPs to translate observed PSD changes into POC fluxes. However, the performance of the ^{234}Th-derived POC fluxes was poor for both the global and regional tuning (Figures 4e-h). Differences between traps and ^{234}Th in the NA have previously been reported at the EXPORTS sampling site and were linked to the persistence of ^{234}Th disequilibrium in the water column prior to sampling (Ceballos-Romero et al., 2016, 2018). Clevenger et al. (2024) suggest that the ^{234}Th profiles sampled during the EXPORTS cruise reflect both an earlier export event in addition to the evolving conditions during the cruise (see also Johnson et al., (2024)). We conclude that the prior export likely contributed to the differences observed in the UVP flux calibration between traps and ^{234}Th in the NA. We see this both in shallow and deeper depths. The ^{234}Th deficit at depth indicates that export had reached deeper waters from the previous time-period. This explains the much higher ^{234}Th-derived POC fluxes compared to traps and UVPs at depth. The export from the first bloom also would influence the calibration of *A* and *B* coefficients using ^{234}Th, at the same time leading to the low predictive power for the regional NA ^{234}Th method. Fluxes based upon ^{234}Th do increase in E3 but are not reflected in the UVP particle fields that are responding more quickly. Therefore, in highly dynamic and non-steady state environments like the NA, changing ^{234}Th distributions do not track the evolving particle fields measured by UVPs.

These observations highlight that when calibrating UVP-based POC fluxes against ^{234}Th, the potential influence of prior export events should be carefully considered, particularly in dynamic regions where past fluxes may dominate thorium deficits. In such scenarios, ^{234}Th may not be a suitable option for calibrating UVP data for POC flux assessment. Future studies combining UVP, trap, and ^{234}Th measurements in regions with minimal prior export could help further evaluate the use of ^{234}Th to improve the accuracy of UVP-based POC flux estimates and enhance our understanding of particle flux dynamics.

5 Next steps

The present results suggest improvements in estimating sinking POC fluxes from in situ imagery requires incorporating more information about the particle field than just size distribution. Eq. (1) shows that POC fluxes could be calculated directly from the size distribution, $N(D)$, only if the size dependence of particle carbon content, $\rho_{POC}(D)$ and its sinking rate, $w_s(D)$, are well constrained. Therefore, it seems important to better characterize these properties as a key pathway towards advancing UVP-based POC flux estimates.

Moving forward, we propose exploring alternative approaches that consider particle traits - such as transparency, shape, and structure -, and geochemical characteristics - such as elemental composition, pigments content, and the nature of organic matter - for more accurate UVP-based POC flux estimates. Next-generation UVPs could also integrate optical measurements, such as particle fluorescence, to provide proxies for some of these properties. Relying on particle size alone neglects the influence of traits that influence sinking behavior and carbon content and thus contributes to export variations over time and depth. For example, the optical properties of particles, particularly their index of refraction, are linked to their carbon content, as

demonstrated in phytoplankton (Stramski, 1999), and this likely holds true for other types of particles such as zooplankton and detritus, where darker particles have been associated with higher carbon content (Durkin et al., 2021). Recent studies also show that transparency and body size can influence particle behavior in the water column, including vertical migration and carbon transport to depth (Barth et al., 2023), while mesozooplankton morphological and taxonomic diversity plays a key role in regional variability of carbon export (Perhirin et al., 2024). Furthermore, sinking velocities have been shown to correlate not only with size but also with particle morphology and aggregate structure, with site-dependent ecological factors and dominant phytoplankton morphologies strongly influencing particle sinking rates and carbon export efficiency (Laurenceau-Cornec et al., 2015) . More recent findings emphasize that mineral ballasting and porosity critically modulate aggregate sinking velocities, challenging classical Stokes' Law assumptions, especially in the mesopelagic zone where organic-to-mineral ratios vary (Laurenceau-Cornec et al., 2020). Together, these findings highlight the need to resolve biological, ecological, and compositional traits beyond the size distribution to enhance our understanding and modeling of particle composition and its role in carbon export.

One alternative approach would be to allow the A and B coefficients to vary with depth to account for changes in particle properties. Initially, we had attempted to vertically stratify the data used to calculate the A and B coefficients, but the results model fits were very poor and that approach was not pursued further. While allowing A and B to vary with depth is a valid empirical approach to capture this variability, it essentially parameterizes unresolved changes in particle properties rather than explicitly resolving them. In contrast, incorporating particle morphological and compositional traits provides a more mechanistic pathway to account for depth-dependent variability. We recommend further studies to compare UVP-based POC flux with estimates from gel traps and include morphological sorting of sinking particles, as introduced in Trudnowska et al., (2021). Such a combined approach could enhance the accuracy of UVP-based POC flux estimates by better distinguishing particle types and identifying dominant morphological groups specific to each site and time.

It is also important to recognize that PSD data reflect standing stocks, which may or may not accurately reflect real POC fluxes. Because large variability between individual UVP profiles is common, averaging multiple profiles is required to reliably estimate local fluxes. Moreover, because UVP profiles represent particle stocks rather than net fluxes, absolute UVP-based POC flux values near the shallowest depths (Figures 3 and 4) can appear unrealistically high and continue to increase toward the surface. Flux estimates in the upper ocean should therefore be interpreted with caution. In this study, fluxes above the mixed layer were excluded to minimize this issue. These limitations highlight the need fornext generation in situ particle imaging systems that incorporate morphological, optical, and geochemical features, enabling more precise and mechanistically informed estimates of particle fluxes and their variability with depth, ultimately advancing our understanding of carbon export dynamics in marine environments.

6 Conclusions

We systematically calibrated large UVP-based PSD data against co-located sediment trap and ^{234}Th flux observations and applied this approach across biogeochemically distinct sites in the NA and NP at both global and regional scales. Our results show that UVP-based POC flux estimates effectively capture broad-scale spatial (NP vs. NA) and temporal (early versus late bloom stages) variations but struggle to resolve finer vertical, temporal, and regional changes. We conclude that in the NP, the limited predictive power reflects small changes in the magnitude of the POC flux observations used to calibrate UVP data and the disproportionate contribution of rare large particles to the flux, while in the NA, sediment trap calibrations outperformed ^{234}Th-based ones due to complexities in ^{234}Th deficits and mismatches between UVP particle stocks and fluxes under non-steady-state conditions. We highlight the need for further calibration studies with ^{234}Th to better assess its utility in variable conditions and suggest exploring UVP use for tracking changes in particle stocks over time rather than assuming that higher stocks reflect higher fluxes.

Despite the value of current calibrations, challenges remain due to imaging size and resolution limits, methodological uncertainties, and variability in the calibration coefficients (*A* and *B*) - which can differ by location, depth, time, and particle size range - sometimes resulting in flux estimate errors exceeding 50%, with variations in A and B across studies sometimes causing order-of-magnitude differences in predicted POC flux (Figure 5). We caution against deriving A and B from a few UVP profiles due to data variability and recommend fitting these coefficients using extensive co-located observations. Where data are limited, for consistency in broader-scale applications using in situ imagery from a size range similar to that discussed in this study (128 µm - 26 mm) and at depths between the mixed layer and 500 m, we suggest users consider the coefficients derived here, specifically the “global approach using traps” for global applications, and the “regional approach using traps NA” for studies focused on the NA region (Table 1). However, we stress that these recommendations are not meant to exclude other approaches. Rather, they reflect the best available fits from our dataset. We encourage further work incorporating more co-located observations across regions and conditions to refine *A* and *B* coefficients for more robust and reliable assessments of sinking particle export fluxes from PSD data.

Acknowledgments

This work was supported by NASA Ocean Biology and Biogeochemistry program, the National Science Foundation Biological and Chemical Oceanography programs and the Woods Hole Oceanographic Institution’s Ocean Twilight Zone study. We greatly acknowledge the cooperation, skill and commitment of the Captains, Crews, Research Technicians and Administrative Staffs of the R/V Roger Revelle (RR1813), R/V Sally Ride (SR1812), RRS James Cook (JC214), RRS Discovery (DY131) and the R/V Sarmiento de Gamboa (SdG2105). This project has received funding from the European Union’s Horizon 2020 research and innovation programme under the Marie Skłodowska-Curie grant agreement No 101032903. RK acknowledges support via a “Make Our Planet Great Again” grant of the French National Research Agency within the “Program d’Investissements d’Avenir”; reference “ANR-19MPGA-0012” and funding from the Heisenberg Programme of the German Science Foundation #KI 1387/5-1.

Data Availability Statement

NASA-funded primary data products are archived at SeaWiFS Bio-optical Archive and Storage System (SeaBASS). All EXPORTS data are being archived under one digital object identifier (DOI: http://dx.doi.org/10.5067/SeaBASS/EXPORTS/DATA001) that further expands into the individual data subsets. NSF-funded. To find out information about all the data collected during the EXPORTS field campaigns, their data repositories and availability, please visit: https://sites.google.com/view/oceanexports/home. All data used in this study, along with MATLAB files for data analysis and visualization, are available under the DOI: https://doi.org/10.6084/m9.figshare.28410668.v3 by Fields & Siegel, 2025.

References

Alldredge, A. (1998). The carbon, nitrogen and mass content of marine snow as a function of aggregate size. *Deep Sea Research Part I: Oceanographic Research Papers*, *45*(4–5), 529–541. https://doi.org/10.1016/S0967-0637(97)00048-4

Alldredge, A. L., & Gotschalk, C. (1988). In situ settling behavior of marine snow. *Limnology and Oceanography*, *33*(3), 339–351. https://doi.org/10.4319/lo.1988.33.3.0339

Amaral, V. J., Lam, P. J., Marchal, O., Roca-Martí, M., Fox, J., & Nelson, N. B. (2022). Particle cycling rates at Station P as estimated from the inversion of POC concentration data. *Elementa: Science of the Anthropocene*, *10*(1), 1415–1428. https://doi.org/10.1525/elementa.2021.00018

Amaral, V. J., Lam, P. J., Marchal, O., & Kenyon, J. A. (2024). Cycling Rates of Particulate Organic Carbon Along the GEOTRACES Pacific Meridional Transect GP15. *Global Biogeochemical Cycles*, *38*(1), e2023GB007940. https://doi.org/10.1029/2023GB007940

Barth, A., Johnson, R., & Stone, J. (2023). Size and transparency influence diel vertical migration patterns in copepods. *Limnology and Oceanography*, *68*(12), 2749–2758. https://doi.org/10.1002/lno.12461

Bisson, K. M., Siegel, D. A., DeVries, T., Cael, B. B., & Buesseler, K. O. (2018). How Data Set Characteristics Influence Ocean Carbon Export Models. *Global Biogeochemical Cycles*, *32*(9), 1312–1328. https://doi.org/10.1029/2018GB005934

Bisson, Kelsey M., Kiko, R., Siegel, D. A., Guidi, L., Picheral, M., Boss, E., & Cael, B. B. (2022). Sampling uncertainties of particle size distributions and derived fluxes. *Limnology and Oceanography: Methods*, 2022. https://doi.org/10.1002/lom3.10524

Boyd, P. W., & Trull, T. W. (2007). Understanding the export of biogenic particles in oceanic waters: Is there consensus? *Progress in Oceanography*, *72*(4), 276–312. https://doi.org/10.1016/j.pocean.2006.10.007

Boyd, Philip W., Claustre, H., Levy, M., Siegel, D. A., & Weber, T. (2019). Multi-faceted particle pumps drive carbon sequestration in the ocean. *Nature*, *568*(7752), 327–335. https://doi.org/10.1038/s41586-019-1098-2

Brzezinski, M. A., Johnson, L., Estapa, M., Clevenger, S., Roca-Martí, M., Romanelli, E., et al.

(2024). Physical Mechanisms Sustaining Silica Production Following the Demise of the Diatom Phase of the North Atlantic Spring Phytoplankton Bloom During EXPORTS. *Global Biogeochemical Cycles*, *38*(7), e2023GB008048. https://doi.org/10.1029/2023GB008048

Buesseler, K. O., Benitez-Nelson, C. R., Moran, S. B., Burd, A., Charette, M., Cochran, J. K., et al. (2006). An assessment of particulate organic carbon to thorium-234 ratios in the ocean and their impact on the application of 234Th as a POC flux proxy. *Marine Chemistry*, *100*(3-4 SPEC. ISS.), 213–233. https://doi.org/10.1016/j.marchem.2005.10.013

Buesseler, Ken O., Bacon, M. P., Kirk Cochran, J., & Livingston, H. D. (1992). Carbon and nitrogen export during the JGOFS North Atlantic Bloom experiment estimated from 234Th: 238U disequilibria. *Deep Sea Research Part A, Oceanographic Research Papers*, *39*(7–8), 1115–1137. https://doi.org/10.1016/0198-0149(92)90060-7

Buesseler, Ken O., Antia, A. N., Chen, M., Fowler, S. W., Gardner, W. D., Gustafsson, O., et al. (2007). An assessment of the use of sediment traps for estimating upper ocean particle fluxes. *Journal of Marine Research*, *65*(3), 345–416. https://doi.org/10.1357/002224007781567621

Buesseler, Ken O., Benitez-Nelson, C. R., Roca-Martí, M., Wyatt, A. M., Resplandy, L., Clevenger, S. J., et al. (2020). High-resolution spatial and temporal measurements of particulate organic carbon flux using thorium-234 in the northeast Pacific Ocean during the EXport Processes in the Ocean from RemoTe Sensing field campaign. *Elementa: Science of the Anthropocene*, *8*(1). https://doi.org/10.1525/elementa.030

Buesseler, Ken O., Boyd, P. W., Black, E. E., & Siegel, D. A. (2020). Metrics that matter for assessing the ocean biological carbon pump. *Proceedings of the National Academy of Sciences of the United States of America*, *117*(18), 9679–9687. https://doi.org/10.1073/pnas.1918114117

Ceballos-Romero, E., Le Moigne, F. A. C., Henson, S., Marsay, C. M., Sanders, R. J., García-Tenorio, R., & Villa-Alfageme, M. (2016). Influence of bloom dynamics on Particle Export Efficiency in the North Atlantic: a comparative study of radioanalytical techniques and sediment traps. *Marine Chemistry*, *186*, 198–210. https://doi.org/10.1016/j.marchem.2016.10.001

Ceballos-Romero, E., De Soto, F., Le Moigne, F. A. C., García-Tenorio, R., & Villa-Alfageme, M. (2018). 234 Th-Derived Particle Fluxes and Seasonal Variability: When Is the SS Assumption Reliable? Insights From a Novel Approach for Carbon Flux Simulation. *Geophysical Research Letters*, *45*(24), 13,414-13,426. https://doi.org/10.1029/2018GL079968

Clements, D. J., Yang, S., Weber, T., McDonnell, A. M. P., Kiko, R., Stemmann, L., & Bianchi, D. (2022). Constraining the Particle Size Distribution of Large Marine Particles in the Global Ocean With In Situ Optical Observations and Supervised Learning. *Global Biogeochemical Cycles*, *36*(5), e2021GB007276. https://doi.org/10.1029/2021GB007276

Clements, D. J., Yang, S., Weber, T., McDonnell, A. M. P., Kiko, R., Stemmann, L., & Bianchi, D. (2023). New Estimate of Organic Carbon Export From Optical Measurements Reveals the

781 Role of Particle Size Distribution and Export Horizon. *Global Biogeochemical Cycles*, *37*(3),
782 1–21. https://doi.org/10.1029/2022GB007633

783 Clevenger, S. J., Benitez-Nelson, C. R., Drysdale, J., Pike, S., Puigcorbé, V., & Buesseler, K. O.
784 (2021). Review of the analysis of 234Th in small volume (2–4 L) seawater samples:
785 improvements and recommendations. *Journal of Radioanalytical and Nuclear Chemistry*,
786 *329*(1). https://doi.org/10.1007/s10967-021-07772-2

787 Clevenger, S. J., Benitez-Nelson, C. R., Roca-Martí, M., Bam, W., Estapa, M., Kenyon, J. A., et al.
788 (2024). Carbon and silica fluxes during a declining North Atlantic spring bloom as part of
789 the EXPORTS program. *Marine Chemistry*, *258*, 104346.
790 https://doi.org/10.1016/j.marchem.2023.104346

791 Cram, J. A., Fuchsman, C. A., Duffy, M. E., Pretty, J. L., Lekanoff, R. M., Neibauer, J. A., et al.
792 (2022). Slow Particle Remineralization, Rather Than Suppressed Disaggregation, Drives
793 Efficient Flux Transfer Through the Eastern Tropical North Pacific Oxygen Deficient Zone.
794 *Global Biogeochemical Cycles*, *36*(1). https://doi.org/10.1029/2021GB007080

795 Drago, L. (2023). *Analyse globale de la pompe à carbone biologique à partir de données en*
796 *imagerie quantitative*. Retrieved from http://www.theses.fr/2023SORUS562/document

797 Durkin, C. A., Buesseler, K. O., Cetinić, I., Estapa, M. L., Kelly, R. P., & Omand, M. (2021). A Visual
798 Tour of Carbon Export by Sinking Particles. *Global Biogeochemical Cycles*, *35*(10),
799 2021.02.16.431317. https://doi.org/10.1029/2021GB006985

800 Eppley, R. W., & Peterson, B. J. (1979). Particulate organic matter flux and planktonic new
801 production in the deep ocean. *Nature*, *282*(5740), 677–680.
802 https://doi.org/10.1038/282677a0

803 Erickson, Z. K., Fields, E., Johnson, L., Thompson, A. F., Lilian, A., Asaro, E. A. D., & Siegel, D. A.
804 (2023). Eddy tracking from in situ and satellite observations. *ESS Open Archive*.
805 https://doi.org/10.22541/essoar.167979672.22588418/v1

806 Estapa, M., Buesseler, K., Durkin, C. A., Omand, M., Benitez-Nelson, C. R., Roca-Martí, M., et al.
807 (2021). Biogenic sinking particle fluxes and sediment trap collection efficiency at Ocean
808 Station Papa. *Elementa*, *9*(1). https://doi.org/10.1525/elementa.2020.00122

809 Fender, C. K., Kelly, T. B., Guidi, L., Ohman, M. D., Smith, M. C., & Stukel, M. R. (2019).
810 Investigating Particle Size-Flux Relationships and the Biological Pump Across a Range of
811 Plankton Ecosystem States From Coastal to Oligotrophic. *Frontiers in Marine Science*, *6*,
812 603. https://doi.org/10.3389/fmars.2019.00603

813 Fields, E., & Siegel, D. A. (2025). data and code used for On the assessment of sinking particle
814 fluxes from in situ aggregate size distribution observations by Elena Ceballos Romero and
815 others - preprint at https://doi.org/10.31223/X5899D.
816 https://doi.org/10.6084/m9.figshare.28410668.v3

817 Forest, A., Babin, M., Stemmann, L., Picheral, M., Sampei, M., Fortier, L., et al. (2013).
818 Ecosystem function and particle flux dynamics across the Mackenzie Shelf (Beaufort Sea,

819 Arctic Ocean): an integrative analysis of spatial variability and biophysical forcings.
820 *Biogeosciences*, *10*(5), 2833–2866. https://doi.org/10.5194/bg-10-2833-2013

821 Giering, S. L. C., Hosking, B., Briggs, N., & Iversen, M. H. (2020). The Interpretation of Particle
822 Size, Shape, and Carbon Flux of Marine Particle Images Is Strongly Affected by the Choice
823 of Particle Detection Algorithm. *Frontiers in Marine Science*, *7*, 564.
824 https://doi.org/10.3389/fmars.2020.00564

825 Guidi, L., Jackson, G. A., Stemmann, L., Miquel, J. C., Picheral, M., & Gorsky, G. (2008).
826 Relationship between particle size distribution and flux in the mesopelagic zone. *Deep-Sea*
827 *Research Part I: Oceanographic Research Papers*, *55*(10), 1364–1374.
828 https://doi.org/10.1016/j.dsr.2008.05.014

829 Guidi, L., Stemmann, L., Jackson, G. A., Ibanez, F., Claustre, H., Legendre, L., et al. (2009). Effects
830 of phytoplankton community on production, size, and export of large aggregates: A world-
831 ocean analysis. *Limnology and Oceanography*, *54*(6), 1951–1963.
832 https://doi.org/10.4319/lo.2009.54.6.1951

833 Guidi, L., Legendre, L., Reygondeau, G., Uitz, J., Stemmann, L., & Henson, S. A. (2015). A new
834 look at ocean carbon remineralization for estimating deepwater sequestration. *Global*
835 *Biogeochemical Cycles*, *29*(7), 1044–1059. https://doi.org/10.1002/2014GB005063

836 Guidi, L., Chaffron, S., Bittner, L., Eveillard, D., Larhlimi, A., Roux, S., et al. (2016). Plankton
837 networks driving carbon export in the oligotrophic ocean. *Nature*, *532*(7600), 465–470.
838 https://doi.org/10.1038/nature16942

839 Iversen, M. H., Nowald, N., Ploug, H., Jackson, G. A., & Fischer, G. (2010). High resolution
840 profiles of vertical particulate organic matter export off Cape Blanc, Mauritania:
841 Degradation processes and ballasting effects. *Deep-Sea Research Part I: Oceanographic*
842 *Research Papers*, *57*(6), 771–784. https://doi.org/10.1016/j.dsr.2010.03.007

843 Johnson, L., Siegel, D. A., Thompson, A. F., Fields, E., Erickson, Z. K., Cetinic, I., et al. (2024).
844 Assessment of oceanographic conditions during the North Atlantic EXport processes in the
845 ocean from RemoTe sensing (EXPORTS) field campaign. *Progress in Oceanography*, *220*,
846 103170. https://doi.org/10.1016/j.pocean.2023.103170

847 Kiko, R., Biastoch, A., Brandt, P., Cravatte, S., Hauss, H., Hummels, R., et al. (2017). Biological
848 and physical influences on marine snowfall at the equator. *Nature Geoscience*, *10*(11),
849 852–858. https://doi.org/10.1038/NGEO3042

850 Kiko, Rainer, Brandt, P., Christiansen, S., Faustmann, J., Kriest, I., Rodrigues, E., et al. (2020).
851 Zooplankton-Mediated Fluxes in the Eastern Tropical North Atlantic. *Frontiers in Marine*
852 *Science*, *7*(May), 1–21. https://doi.org/10.3389/fmars.2020.00358

853 Kiko, Rainer, Picheral, M., Antoine, D., Babin, M., Berline, L., Biard, T., et al. (2022). A global
854 marine particle size distribution dataset obtained with the Underwater Vision Profiler 5
855 (Discussion). *Earth System Science Data Discussions*, *14*(9), 4315–4337.
856 https://doi.org/10.5194/essd-2022-51

Kriest, I. (2002). Different parameterizations of marine snow in a 1D-model and their influence on representation of marine snow, nitrogen budget and sedimentation. *Deep Sea Research Part I: Oceanographic Research Papers*, *49*(12), 2133–2162. https://doi.org/10.1016/S0967-0637(02)00127-9

De La Rocha, C. L., & Passow, U. (2007). Factors influencing the sinking of POC and the efficiency of the biological carbon pump. *Deep-Sea Research Part II: Topical Studies in Oceanography*, *54*(5–7), 639–658. https://doi.org/10.1016/j.dsr2.2007.01.004

Laurenceau-Cornec, E., Trull, T., Davies, D., De La Rocha, C., & Blain, S. (2015). Phytoplankton morphology controls on marine snow sinking velocity. *Marine Ecology Progress Series*, *520*, 35–56. https://doi.org/10.3354/meps11116

Laurenceau-Cornec, E. C., Le Moigne, F. A. C., Gallinari, M., Moriceau, B., Toullec, J., Iversen, M. H., et al. (2020). New guidelines for the application of Stokes' models to the sinking velocity of marine aggregates. *Limnology and Oceanography*, *65*(6), 1264–1285. https://doi.org/10.1002/lno.11388

Logan, B. E., & Kilps, J. R. (1995). Fractal dimensions of aggregates formed in different fluid mechanical environments. *Water Research*, *29*(2), 443–453. https://doi.org/10.1016/0043-1354(94)00186-B

Logan, B. E., & Wilkinson, D. B. (1990). Fractal geometry of marine snow and other biological aggregates. *Limnology and Oceanography*, *35*(1), 130–136. https://doi.org/10.4319/lo.1990.35.1.0130

Lombard, F., & Kiørboe, T. (2010). Marine snow originating from appendicularian houses: Age-dependent settling characteristics. *Deep Sea Research Part I: Oceanographic Research Papers*, *57*(10), 1304–1313. https://doi.org/10.1016/j.dsr.2010.06.008

McDonnell, A. M. P., & Buesseler, K. O. (2010). Variability in the average sinking velocity of marine particles. *Limnology and Oceanography*, *55*(5), 2085–2096. https://doi.org/10.4319/lo.2010.55.5.2085

McNair, H. M., Meyer, M. G., Lerch, S. J., Maas, A. E., Stephens, B. M., Fox, J., et al. (2023). Quantitative analysis of food web dynamics in a low export ecosystem. *BioRxiv*, 2023.03.17.532807. https://doi.org/10.1101/2023.03.17.532807

Perhirin, M., Gossner, H., Godfrey, J., Johnson, R., Blanco-Bercial, L., & Ayata, S. (2024). Morphological and taxonomic diversity of mesozooplankton is an important driver of carbon export fluxes in the ocean. *Molecular Ecology Resources*, *24*(2), e13907. https://doi.org/10.1111/1755-0998.13907

Picheral, M., Guidi, L., Stemmann, L., Karl, D. M., Iddaoud, G., & Gorsky, G. (2010). The underwater vision profiler 5: An advanced instrument for high spatial resolution studies of particle size spectra and zooplankton. *Limnology and Oceanography: Methods*, *8*(SEPT), 462–473. https://doi.org/10.4319/lom.2010.8.462

Picheral, M., Catalano, C., Brousseau, D., Claustre, H., Coppola, L., Leymarie, E., et al. (2022).

895 <scp>The Underwater Vision Profiler 6: an imaging sensor of particle size spectra and
896 plankton, for autonomous and cabled platforms</scp>. *Limnology and Oceanography:*
897 *Methods*, *20*(2), 115–129. https://doi.org/10.1002/lom3.10475

898 Ramondenc, S., Madeleine, G., Lombard, F., Santinelli, C., Stemmann, L., Gorsky, G., & Guidi, L.
899 (2016). An initial carbon export assessment in the Mediterranean Sea based on drifting
900 sediment traps and the Underwater Vision Profiler data sets. *Deep-Sea Research Part I:*
901 *Oceanographic Research Papers*, *117*, 107–119. https://doi.org/10.1016/j.dsr.2016.08.015

902 Romanelli, E., Giering, S. L. C., Estapa, M., Siegel, D. A., & Passow, U. (2024). Can intense storms
903 affect sinking particle dynamics after the North Atlantic spring bloom? *Limnology and*
904 *Oceanography*, 2024.01.11.575202. https://doi.org/10.1002/lno.12723

905 Savoye, N., Benitez-Nelson, C., Burd, A. B., Cochran, J. K., Charette, M., Buesseler, K. O., et al.
906 (2006). 234Th sorption and export models in the water column: A review. *Marine*
907 *Chemistry*, *100*(3-4 SPEC. ISS.), 234–249. https://doi.org/10.1016/j.marchem.2005.10.014

908 Seber, G. A. F., & Wild, C. J. (2003). *Nonlinear Regression*. *Wiley*. New York: Wiley. Retrieved
909 from http://as.wiley.com/WileyCDA/WileyTitle/productCd-0471471356.html

910 Sheldon, R. W., Prakash, A., & Sutcliffe, H. (1972). The size distribution of particles in the ocean.
911 *Limnology and Oceanography*, *XVII*(MAY), 327–340.

912 Siegel, D. A., Burd, A. B., Estapa, M. L., Fields, E., Johnson, L., Passow, U., et al. (2025). Assessing
913 marine snow dynamics during the demise of the North Atlantic spring bloom using in situ
914 particle imagery. *Global Biogeochemical Cycles*, 39,
915 e2025GB008676. https://doi.org/10.1029/2025GB008676 Siegel, D. A., Fields, E., &
916 Buesseler, K. O. (2008). A bottom-up view of the biological pump: Modeling source funnels
917 above ocean sediment traps. *Deep-Sea Research Part I: Oceanographic Research Papers*,
918 *55*(1), 108–127. https://doi.org/10.1016/j.dsr.2007.10.006

919 Siegel, David A., Buesseler, K. O., Behrenfeld, M. J., Benitez-Nelson, C. R., Boss, E., Brzezinski, M.
920 A., et al. (2016). Prediction of the export and fate of global ocean net primary production:
921 The exports science plan. *Frontiers in Marine Science*, *3*(MAR).
922 https://doi.org/10.3389/fmars.2016.00022

923 Siegel, David A., Cetinić, I., Graff, J. R., Lee, C. M., Nelson, N., Perry, M. J., et al. (2021). An
924 operational overview of the EXport Processes in the Ocean from RemoTe Sensing
925 (EXPORTS) Northeast Pacific field deployment. *Elementa: Science of the Anthropocene*,
926 *9*(1). https://doi.org/10.1525/elementa.2020.00107

927 Siegel, David A., DeVries, T., Cetinić, I., & Bisson, K. M. (2023a). Quantifying the Ocean's
928 Biological Pump and Its Carbon Cycle Impacts on Global Scales. *Annual Review of Marine*
929 *Science*, *15*(1), 329–356. https://doi.org/10.1146/annurev-marine-040722-115226

930 Siegel, David A., Cetinic, I., Thompson, A. F., Nelson, N. B., Sten, M., Omand, M., et al. (2023b).
931 *EXport Processes in the Ocean from RemoTe Sensing (EXPORTS) North Atlantic sensor*
932 *calibration and intercalibration documents*. https://doi.org/10.1575/1912/66998

Soucie, J. E. S., Sosik, H. M., Girdhar, Y., Shalapyonok, A., Peacock, E., & Johnson, L. Spatiotemporal Topic Modeling Reveals Storm-Driven Advection and Stirring Control Plankton Community Variability in an Open Ocean Eddy. *Authorea Preprints*. https://doi.org/10.22541/ESSOAR.171415914.42561749/V1

Stamieszkin, K., Steinberg, D. K., & Maas, A. E. (2021). Fecal pellet production by mesozooplankton in the subarctic Northeast Pacific Ocean. *Limnology and Oceanography*, *66*(7), 2585–2597. https://doi.org/10.1002/lno.11774

Steinberg, D. K., Stamieszkin, K., Maas, A. E., Durkin, C. A., Passow, U., Estapa, M. L., et al. (2023). The Outsized Role of Salps in Carbon Export in the Subarctic Northeast Pacific Ocean. *Global Biogeochemical Cycles*, *37*(1), e2022GB007523. https://doi.org/10.1029/2022GB007523

Stemmann, L., & Boss, E. (2012). Plankton and particle size and packaging: From determining optical properties to driving the biological pump. *Annual Review of Marine Science*, *4*(1), 263–290. https://doi.org/10.1146/annurev-marine-120710-100853

Stramski, D. (1999). Refractive index of planktonic cells as a measure of cellular carbon and chlorophyll a content. *Deep Sea Research Part I: Oceanographic Research Papers*, *46*(2), 335–351. https://doi.org/10.1016/S0967-0637(98)00065-X

Trudnowska, E., Lacour, L., Ardyna, M., Rogge, A., Irisson, J. O., Waite, A. M., et al. (2021). Marine snow morphology illuminates the evolution of phytoplankton blooms and determines their subsequent vertical export. *Nature Communications*, *12*(1), 2816. https://doi.org/10.1038/s41467-021-22994-4

Turner, J. T. (2015). Zooplankton fecal pellets, marine snow, phytodetritus and the ocean's biological pump. *Progress in Oceanography*, *130*(1), 205–248. https://doi.org/10.1016/j.pocean.2014.08.005

Supporting Information for

On the assessment of sinking particle fluxes from in situ aggregate size distribution observations

Contents of this file

Text S1

Table S1

Figures S1 to S4

Text S1.

UVP: data and calibration

1. UVP data

UVPs were deployed during EXPORTS to estimate the true particle population by means of measuring the PSD in the water column. Two UVP5s in EXPORTS-NP (serial numbers SN 201 and 207, see calibration report for more details, Siegel et al. (2023)), and three in EXPORTS-NA (SN 201, 203 and 205) provided high quality measurements of the abundance, composition, and size distribution of suspended particles (including live organisms) in the water column. During EXPORTS-NP, UVP5 SN207 captured data during CTD downcast during 138 of 144 casts of cruise *SR1812*; the unsuccessful casts did not have a clear cause as to why the instrument did not work as programmed. During cruise *RR1813*, UVP5 SN201 provided a total of 84 profiles of particle size distribution as part of the activities of the survey ship. During EXPORTS-NA, the UVP5s captured data during CTD downcast during 112, 69 and 13 casts of cruises DY131 (SN201), JC214 (SN203), and SdG2105 (SN205) respectively.

2. UVPs intercalibration

Calibration of the UVP5 pixel to millimeter conversion is done by the Laboratoire d'Océanographie de Villefranche sur Mer (LOV). This involves quantifying the illuminated volume and determining the appropriate conversion between imaged particle area in pixels and mm^2 (Picheral et al., 2010). The latter is initially done by measuring the size of particles with a microscope and their corresponding pixel area in the UVP image (dropping particles one at a time in the field of view of the camera) in order to determine the raw pixel size (pixels mm^{-1}). The instruments used during each EXPORTS cruise were sent together to the manufacturer for pre-cruise calibration, where each instrument underwent an in situ inter-calibration against the same reference UVP in the Bay of Villefranche, France. From this intercalibration, a power law relationship of the form $S_m = Aa \times S_p^{Exp}$ is used to derive calibration coefficients *Aa* and *Exp* for each instrument that minimize the log-transformed differences between the particle area in pixels (S_p) and particle area in mm^2 (S_m). These calibration coefficients are reported in the calibration documents and used to calculate the size of each particle imaged by the UVP during the EXPORTS program (see Siegel et al. (2023) for UVP calibration report).

As several UVP units were used, an intercalibration procedure was developed to allow comparability of data from these units (Siegel et al., 2023). Very briefly, the intercalibration procedure is based on a comparison between one or several reference units and the units to be calibrated. UVP-based PSD observations are intercompared using nearby in time and space casts. During EXPORTS-NP, UVP serial number 207 on the Survey Ship consistently overestimated the particle concentrations measured by UVP serial number 201 on the Process Ship for unknown reasons, despite being intercalibrated to a reference UVP prior to the cruise. These differences were observed across most size and depth bins. However, due to the limited number of intercomparison profiles and the fact that the instruments were not sampling the exact same parcels of water (deployed from separate ships), no specific corrections or adjustments were applied for EXPORTS-NP. An intermittent lighting issue, where at least one lighting unit failed to illuminate, was also noted for both UVP units. Bad images resulting from this issue were filtered out of the original database using a procedure developed by LOV. During EXPORTS-NA, four match-up casts were identified between *DY131* and *JC214* and two between the *DY131* and *SdG2105*. While *DY131* and *SdG2105* UVPs showed very similar PSD data; *JC214* PSD data were considerably lower, particularly for the smaller size bins, and had known issues related to the discovery of a zip tie in the field of view. *DY131* PSD data were used as the "standard" due to their consistent availability throughout the entire cruise and broad consistency with *SdG2105* PSD results. Linear regression models were employed to correct the *JC214* PSD data to best match the *DY131* data for the size bins with a linear correlation (r^2) value exceeding 0.8. The data were subsequently vertically binned into 25-m bins to enhance statistics for the largest size bins without significantly altering the values of the smaller bin corrections. The resulting remapped data show consistency among the three UVP-PSD data sources, offering a data set to explore the relationships among particle distributions and export fluxes.

	NP			NA		
epoch	traps	UVP	234Th & UVP	traps	UVP	234Th & UVP
E1	11	37	17	7	17	5
E2	11	34	20	5	18	8
E3	10	73	18	6	9	9

Table S1. Summary of the number of UVP profiles, sediment traps, and ^{234}Th profiles used in the regional matchups by epoch.

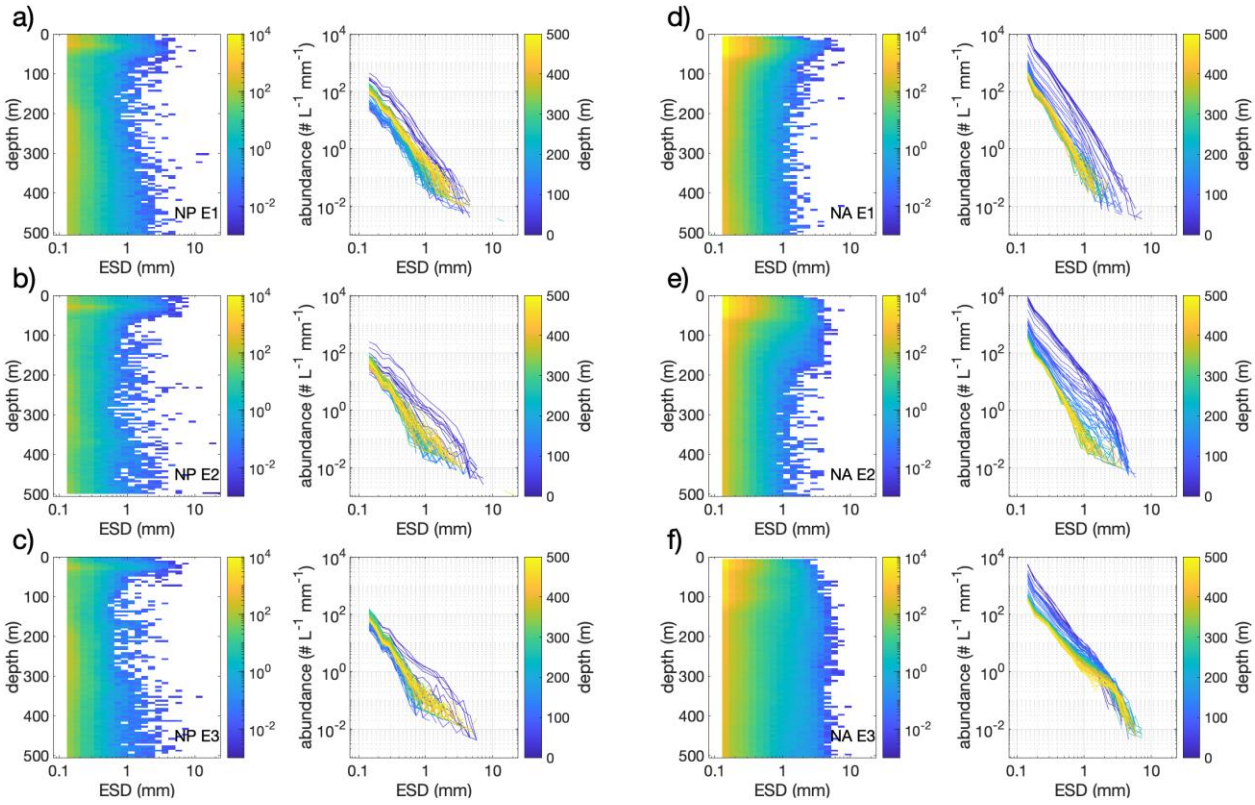

Figure S1. Observed particle size distribution (PSD) of in situ particles plotted against aggregate equivalent spherical diameter (ESD, mm) for the (a-c) NP and (d-f) NA experiments. For each panel, the figure on the left shows ESD versus depth, the color bar indicates particle abundance for each size (in # L^{-1} mm^{-1}, logarithmic scale). Red indicates a higher number of particles than blue; the figure on the right shows ESD versus abundance, the color bar indicates depth (in m). A random profile is shown for each of the epochs (E1, E2, and E3).

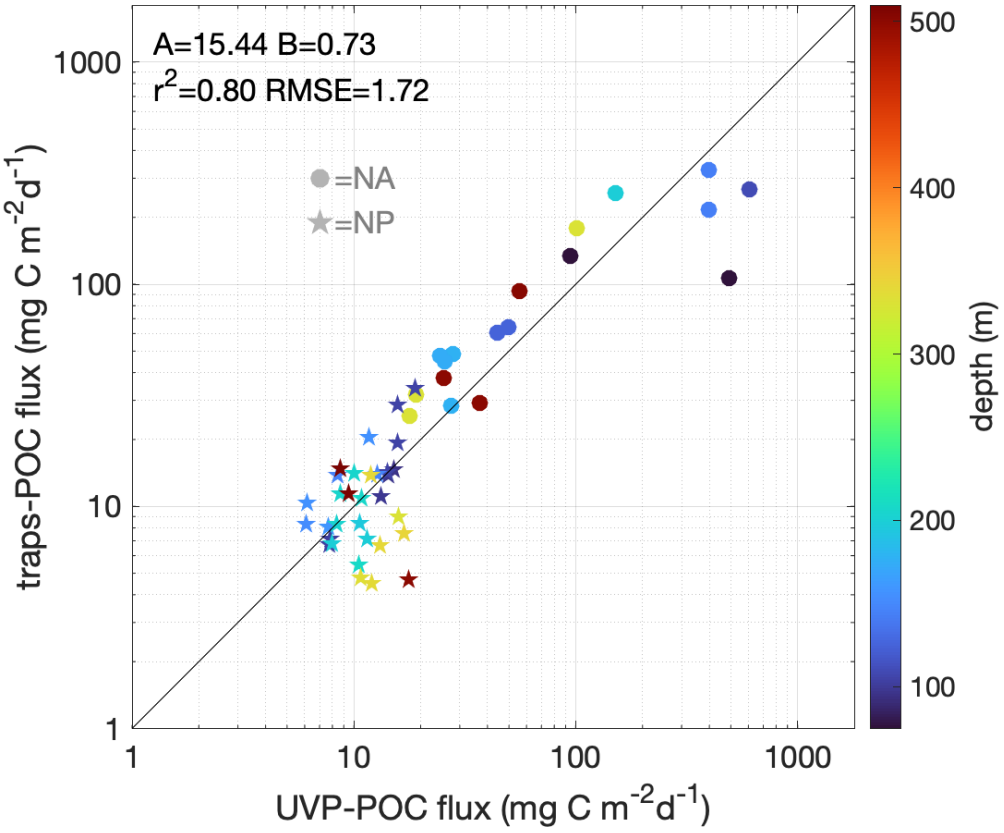

Figure S2. Detailed figure for our reproduction of the "global UVP method" from Guidi et al., (2008) with the EXPORTS data set (i.e., global approach using traps with 8 bins: 250 µm – 1.5 mm). Color coding indicates depth.

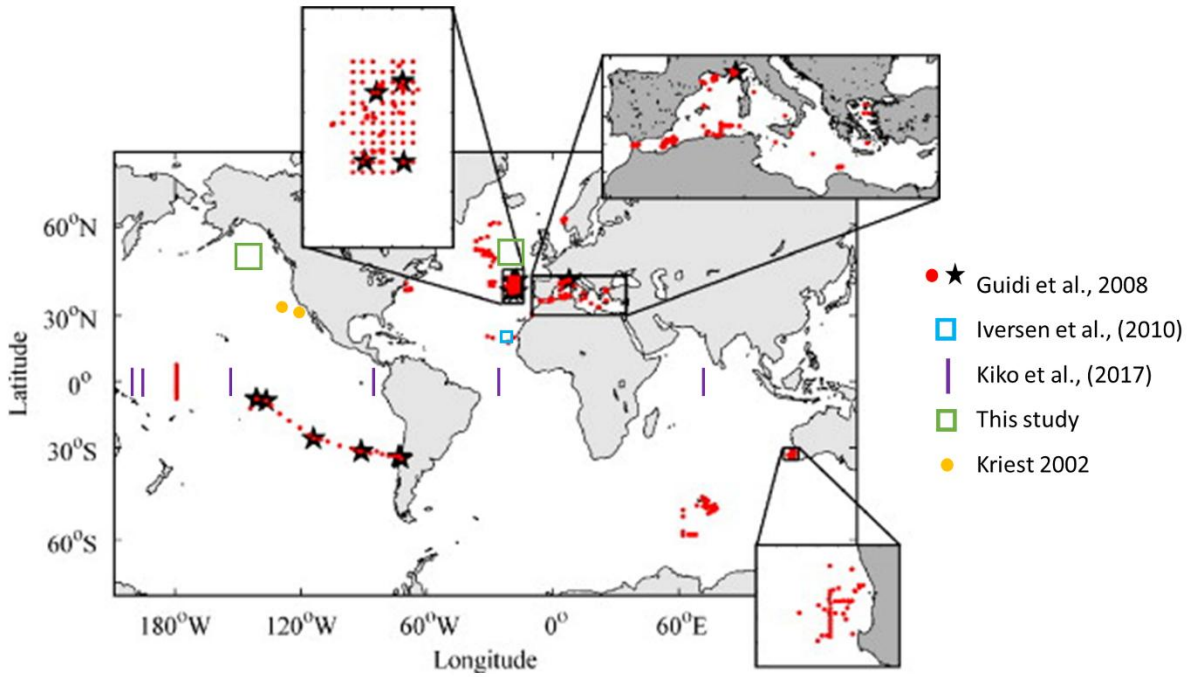

Figure S3. Modified map based on Figure 1 from Guidi et al., (2008) to include the sampling sites of the studies summarized in Table 1 that use observations to estimate A and B coefficients. The map features: red dots and black stars to indicate UVP and trap data respectively from Guidi et al., (2008), blue square to show study site from Iversen et al., (2010), sampled with deep sediment traps and an underwater camera (ParCa type), purple lines to indicate transits from Kiko et al., (2017) with UVP data, and green squares to denote sampling locations from this study, which included UVP data, and traps and ^{234}Th measurements. Kriest, (2002) estimated A and B coefficients based on a variety of observations about the mass and sinking speed of marine snow in relationship to its diameter from Alldredge (1998) and Smith et al., (1998). Sampling locations of these observations are indicated with yellow and orange circles respectively. Note that observations from Alldredge (1998) are based on undisturbed aggregates of marine snow hand-collected at depths of 10 to 20 m in the Santa Barbara Channel (California, USA), while those from Smith et al., (1998) are based on large detrital aggregates collected from the seafloor at an abyssal site in the NE Pacific. The observations used by Clements et al., (2023) are very extensive, and we therefore refer to the original publications for detailed sampling sites. Sediment traps and ^{234}Th locations used can be found in Figure 2 in Bisson et al., (2018), while the UVP data are available in Figure 2 in Kiko et al., (2022). The profiles of PSD observations used in Bisson et al., (2022) come from the first version of the UVP compilation by Kiko et al., (2022) accessible in (Kiko et al. (2021).

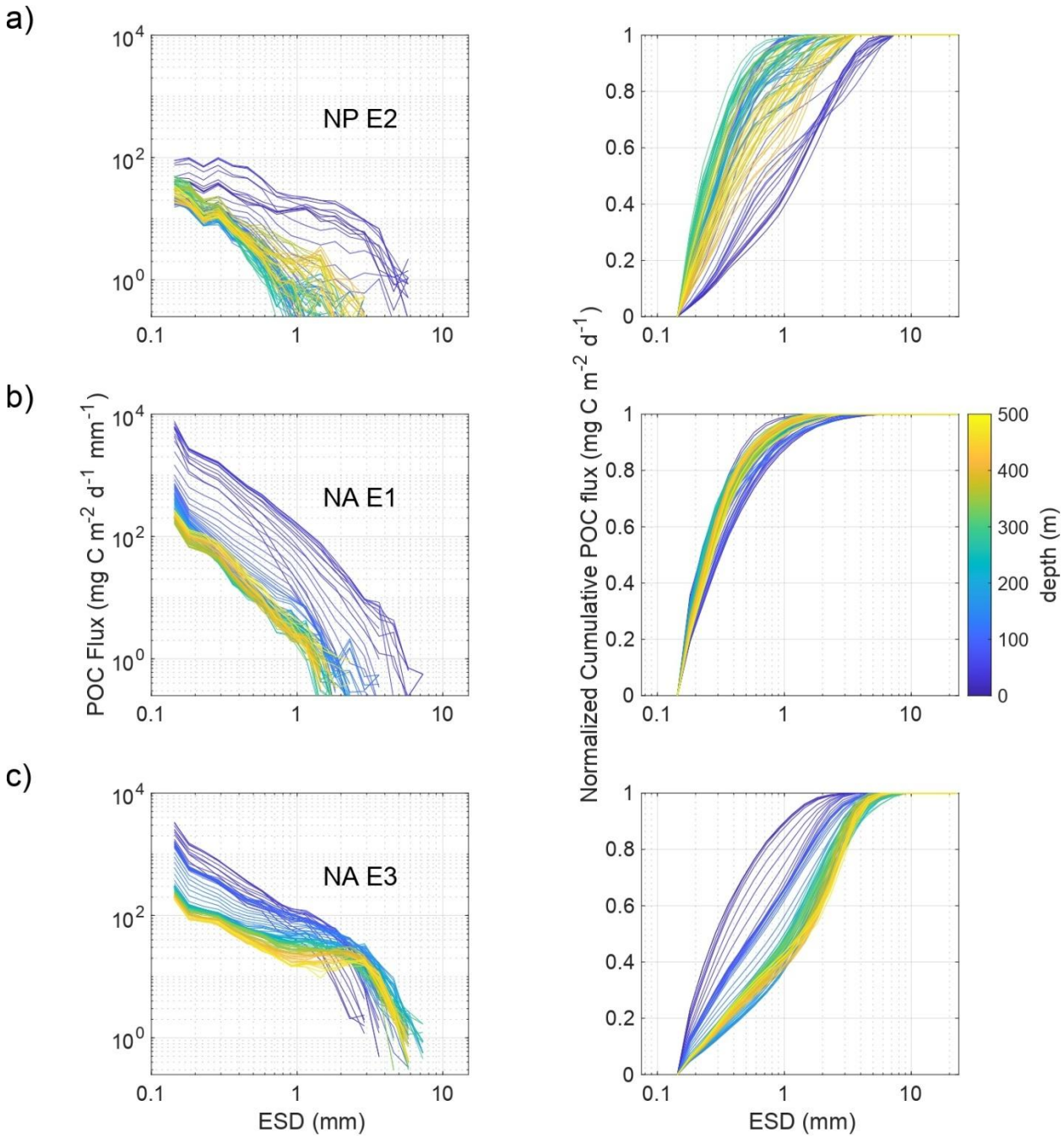

Figure S4. Size dependence of globally modeled trap POC fluxes (a–c) as a function of equivalent spherical diameter (ESD, mm) across depths for NP (a) and NA (b–c). The color bar indicates depth (in m). The right-hand panels show the corresponding normalized cumulative POC flux for each case.

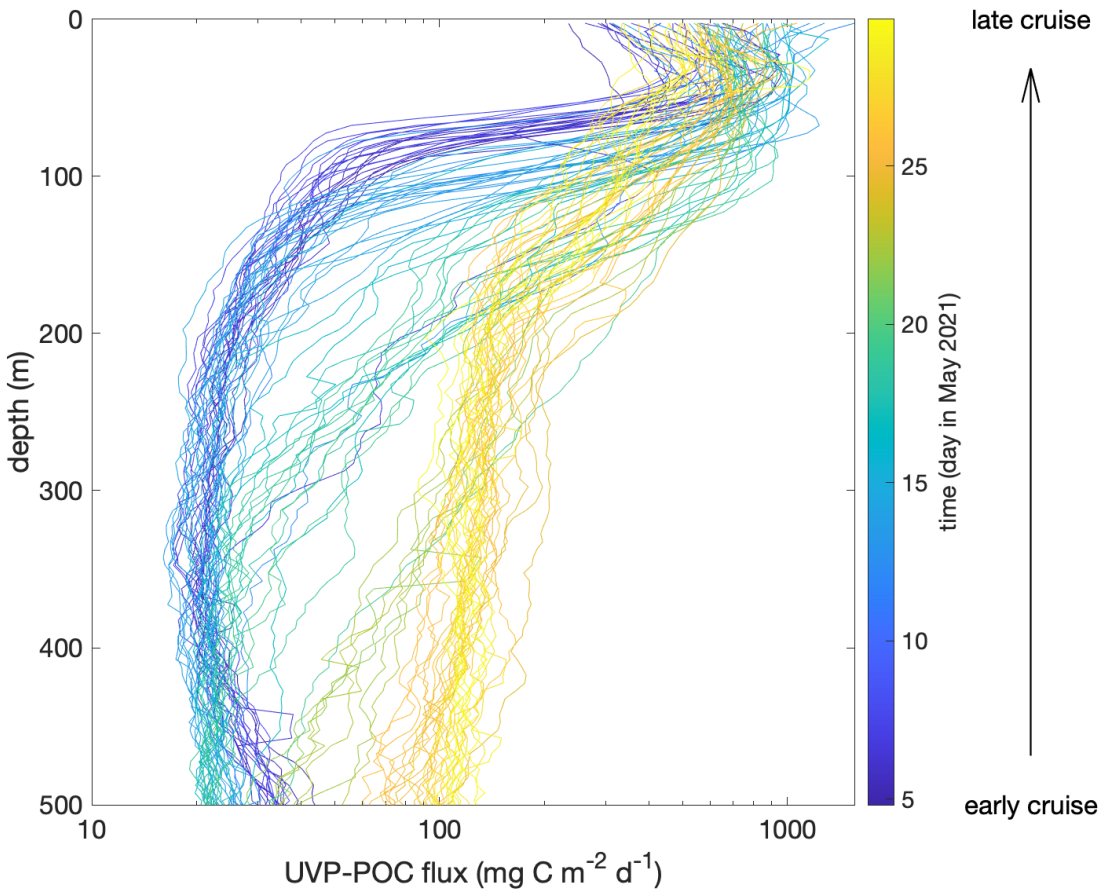

Figure S5. Vertical profiles of POC fluxes for the global approach in the NA using trap data (Figure 4a in the main text) featuring color as time, with blue corresponding to early in the cruise and yellow with late in the cruise.